


















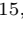
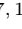



# Catching Disguised Transients with ASTRANet: Anomaly-Aware Spectroscopic Classification and Conformal Calibration

Argyro Sasli <sup>1,2,\*</sup> Maojie Xu <sup>3,2</sup> Alexandra Junell <sup>1,2</sup> Hailey Markoff<sup>1,2</sup> Avyukt Raghuvanshi <sup>1,2</sup> Felipe Fontinele Nunes <sup>1,2</sup> Theophile Jegou Du Laz <sup>4,2</sup> Jesper Sollerman <sup>5</sup> Christoffer Fremling <sup>6,7</sup> Drew Oldag <sup>8</sup> Antoine Le Calloch <sup>1,2</sup> Sushant Sharma Chaudhary <sup>1,2</sup> Sneha Maharjan <sup>1</sup> Maxine West <sup>8</sup> Benny Border<sup>1,2</sup> Nabeel Rehentulla <sup>9,10,11</sup> Richard Dekany <sup>6</sup> Joahan Castaneda Jaimes <sup>12</sup> Russ R. Laher <sup>13</sup> Reed Riddle <sup>6</sup> Mansi M. Kasliwal <sup>14</sup> Matthew J. Graham <sup>15,2</sup> Ashish A. Mahabal <sup>7,16</sup> and Michael W. Coughlin <sup>1,2</sup>

<sup>1</sup>*School of Physics and Astronomy, University of Minnesota, Minneapolis, MN 55455, USA*

<sup>2</sup>*NSF Institute on Accelerated AI Algorithms for Data-Driven Discovery (A3D3)*

<sup>3</sup>*Department of Computer Science & Engineering,  
University of Minnesota, Minneapolis, MN 55455, USA*

<sup>4</sup>*Division of Physics, Mathematics and Astronomy, California Institute of Technology,  
1200 E California Blvd., Pasadena, CA 91125, USA*

<sup>5</sup>*Department of Astronomy, Stockholm University, 10691 Stockholm, Sweden*

<sup>6</sup>*Caltech Optical Observatories, California Institute of Technology, Pasadena, CA 91125, USA*

<sup>7</sup>*Division of Physics, Mathematics and Astronomy,  
California Institute of Technology, Pasadena, CA 91125, USA*

<sup>8</sup>*Dept. of Astronomy & the DiRAC Institute, University of Washington, Box 351580, Seattle, WA 98195, USA*

<sup>9</sup>*Department of Physics and Astronomy, Northwestern University, 2145 Sheridan Road, Evanston, IL 60208, USA*

<sup>10</sup>*Center for Interdisciplinary Exploration and Research in Astrophysics  
(CIERA), 1800 Sherman Ave., Evanston, IL 60201, USA*

<sup>11</sup>*NSF-Simons AI Institute for the Sky (SkAI), 172 E. Chestnut St., Chicago, IL 60611, USA*

<sup>12</sup>*Division of Physics, Mathematics and Astronomy, California Institute of Technology,  
1200 E. California Blvd., Pasadena, CA 91125, USA*

<sup>13</sup>*IPAC, California Institute of Technology, 1200 E. California Blvd., Pasadena, CA 91125, USA*

<sup>14</sup>*Division of Physics, Mathematics, and Astronomy,  
California Institute of Technology, Pasadena, CA 91125, USA*

<sup>15</sup>*Cahill Center for Astrophysics, California Institute of Technology, Pasadena, CA 91125, USA*

<sup>16</sup>*Center for Data Driven Discovery, California Institute of Technology, Pasadena, CA 91125, USA*

Time-domain surveys discover thousands of transients per year, but the spectroscopic identification of rare and physically peculiar objects remains rate-limited by closed-set classifiers that confidently assign every input to a known class – including spectra that genuinely belong to no known class. We present the ASTRANet framework, a confidence-aware infrastructure for spectroscopic transient classification built around three coupled modules: a hierarchical spectral classifier that operates directly on observer-frame spectra without requiring host-galaxy redshift or spectral phase as inputs; an anomaly detection layer (ASTRANet-Sentinel) that non-linearly combines 16 embedding-space anomaly scores spanning four physically motivated families; and a conformal uncertainty quantification layer (ASTRANet-CP). We validate the framework on a held-out evaluation set of 289 rare and out-of-taxonomy transients spanning 11 classes deliberately excluded from training, chosen to span the full physical diversity of the rare-anomaly population: AGN-related outliers, GRB-related events, gap transients, novae, and peculiar supernovae. Through five astrophysically distinct failure modes of closed-set classifiers, we show that classifier-internal uncertainty and embedding-based anomaly detection are structurally complementary axes of confidence rather than alternative implementations of the same estimator. We further introduce AD-stratified Mondrian conformal prediction (AD-MCP) within ASTRANet-CP, achieving uniform conditional coverage across anomaly-score strata where vanilla Mondrian under-covers in the operational regime. This establishes the methodological infrastructure for confidence-aware spectroscopic discovery in the Vera C. Rubin Observatory era.

## I. INTRODUCTION

Time-domain surveys discover  $\sim 10^5$  transient candidates per year [ZTF; 1–5] heading to  $\sim 10^6$ /year at LSST depth [6], of which only a tiny fraction can receive spectroscopic follow-up.

The bottleneck is not only in taking spectra — not even the SED Machine [7, 8] and similar rapid spectrographs have been able to close that gap, since even SEDM can observe only a small fraction of ZTF transients, far short of the LSST scale — but increasingly in *deciding which spectra deserve deeper observations* and in *recognising* when an observed spectrum represents something genuinely novel. This second decision is the substrate of discovery: most peculiar transient classes – Type Iax [9], Ca-rich [10], Fast Blue Optical Transients [FBOTs];

\* [asasli@umn.edu](mailto:asasli@umn.edu)

11, 12], Intermediate Luminosity Red Transients [ILRTs; 13] – were identified not by template-matching but by recognizing that the spectra did not fit known templates well enough. Deep classifiers [14–17] excel on common classes but are typically deployed *closed-set*: every input is assigned to a training class with a softmax probability regardless of whether the input belongs to one. The result is a specific dangerous failure mode – high-confidence wrong answers [18–20] – which the architectural features that make these classifiers accurate on common classes actively conceal. Existing remedies in astronomy focus on photometric light curves [21–24] and almost always deploy single-score pipelines, while uncertainty quantification (UQ) is treated as a separate axis from anomaly detection (AD). We argue these axes must be co-equal outputs of a single confidence-aware framework, and that for spectroscopy specifically, no single anomaly-score family suffices because the failure modes are themselves physically diverse. Throughout this work the catalog classifications – Blazar, Ca-rich, ILRT, FBOT, etc. – are treated as reference classifications; the failure modes we document are what closed-set models produce when shown these correctly-labelled spectra.

We present **ASTRANet**<sup>1</sup>, a confidence-aware framework organised into three coupled modules. A hierarchical spectral classifier operates on *observer-frame* spectra, treating host-galaxy redshift and spectral phase as optional metadata injected via FiLM [25] with validity bits and random masking during training – never requiring either at inference, in contrast to prior multi-class deep spectroscopic classifiers that rest-frame their inputs and consume an estimated redshift (i.e., see [26]) (Muthukrishna et al. 2019; Xu et al. 2025). Binary classifiers such as SNIascore [14] likewise operate without explicit redshift input, but ASTRANet is, to our knowledge, the first fine-grained, multi-class classifier to do so on observer-frame spectra. An anomaly-detection layer (**ASTRANet-Sentinel**) non-linearly combines 16 embedding-space scores spanning uncertainty, distance, density, and hybrid families into a single cross-family AD score. A conformal uncertainty layer (**ASTRANet-CP**) produces per-spectrum calibrated p-value, adaptive prediction set, per-class ensemble probability intervals, and aleatoric/epistemic decomposition in one forward pass, with distribution-free finite-sample calibration guarantees that remain valid under arbitrary distribution shift.

*a. Two key findings shape the design.* First, the failure modes of closed-set spectroscopic classifiers are not a uniform softmax-overconfidence phenomenon but separate into *five physically distinct regimes* – continuum-disguised AGN-class events, spectroscopic disguise within physical neighbours, continuum-dominated mis-classifications, legitimately ambiguous progenitor regimes, and far-out-of-distribution events.

Each regime manifests in a different anomaly-score signature; no single family covers all five. The cross-family non-linear combiner is required not as engineering overhead but *because the physics is diverse* (Sec. II). Second, classifier-internal uncertainty and embedding-based anomaly detection are *structurally complementary* axes of confidence: the former dominates on in-distribution boundary errors, the latter on out-of-distribution disguise where the ensemble is confidently wrong. They flag largely disjoint failure populations and should be deployed simultaneously, not interchangeably (Sec. VI F).

*b. What this enables.* This combination unlocks four science capabilities that closed-set pipelines do not. (i) *Real-time spectroscopic triage on freshly discovered transients*: classification, anomaly detection, and uncertainty quantification all operate without host redshift or spectral phase, removing a delay specific to multi-class template- and rest-frame-based classification, rather than the spectrum-acquisition step itself. (ii) *Retrospective recovery of disguised populations* from the existing ZTF archive: Blazars mislabeled as CVs, Ca-rich transients absorbed into Ib/c, novae absorbed into CV – populations that closed-set pipelines silently lose at substantial rates. (iii) *Calibrated, defensible follow-up allocation*, where operators set explicit false-alarm budgets rather than triaging on uncalibrated classifier confidence. (iv) *A discovery channel for the next gap-transient class*: structurally anomalous spectra are flagged on embedding geometry rather than recognised only post-hoc. The framework is being prepared for offline production integration with the ZTF BOOM broker [27] ahead of a planned spectroscopic follow-up campaign reported in companion work [28]; we argue infrastructure of this kind will be required, not optional, at LSST depth.

*c. Contributions.*

1. A *redshift-free, phase-free, observer-frame* architecture for spectroscopic transient classification (Sec. IV A). To our knowledge **ASTRANet** is the first spectroscopic transient classifier that achieves competitive accuracy without rest-framing any spectrum and without requiring redshift or phase at inference, removing the principal real-time dependency of existing classifiers.
2. A characterisation of *five physically distinct failure modes* of closed-set spectroscopic classifiers (Sec. II), each linked to a specific anomaly-score signature and a specific astrophysical regime. This taxonomy is, to our knowledge, new and motivates the cross-family AD design directly from physics. We show empirically that cross-family non-linear combination is not redundant with single-family scoring – a substantial majority of the framework’s detections come from spectra no single family recognises (Sec. V C).
3. A *distribution-free uncertainty quantification layer* (**ASTRANet-CP**, Sec. VI) via Mondrian conformal

<sup>1</sup>ASTRANet: Anomaly-aware Spectroscopic TRAnsient Network; the stem also echoes the Greek *ástra* (“stars”).

prediction with empirically validated coverage. The per-sample  $p_{\text{wrong}} = 1 - p_{\text{M}}$  is a distribution-free, finite-sample-calibrated probability that the prediction is mistaken, valid under arbitrary distribution shift provided the calibration set remains exchangeable. The framework exposes a structural complementarity between classifier-internal UQ and the cross-family AD layer that supports *AD-orthogonal abstention* (Sec. VI G).

4. *AD-stratified Mondrian Conformal Prediction* (AD-MCP; Sec. VI H), extending atypicality-stratified conformal calibration [29] to a learned cross-family anomaly ensemble crossed with predicted class, recovering uniform conditional coverage in the high-AD operational regime where vanilla Mondrian under-covers.
5. A deployment-ready pipeline with three selectable operating regimes (score-averaged anchor, per-seed detectors, seed-union), evaluated under a leakage-free  $k$ -fold protocol on a diverse 11-class rare and 7-class general transient set.

The remainder of this paper is organised as follows. Section II establishes the failure-mode taxonomy empirically. Section III describes the dataset. Section IV presents the framework: classifier, deep ensemble, 16 anomaly scores, and non-linear combiner. Section V validates the framework on the rare-anomaly evaluation set. Section VI extends the framework to distribution-free uncertainty quantification. Section VII presents physically interpretable case studies of the five failure modes. Section VIII discusses deployment, limitations, and the path to the LSST era.

## II. A FAILURE-MODE TAXONOMY OF SPECTROSCOPIC CLASSIFIERS

Before introducing the framework, we establish empirically that the failure modes of closed-set spectroscopic classifiers are *physically structured* rather than uniform. This observation shapes the design of the framework: a single uncertainty score that treats all failures alike will catch some failure modes and miss others; a cross-family combiner that integrates evidence from embedding geometry, density, hierarchical-head disagreement, and softmax confidence is necessary because the failure modes themselves are diverse.

We identify five regimes from the held-out evaluation set (Sec. III, Table XIV). Each regime is anchored by at least one representative ZTF object whose true classification is independently established, and each maps to a single dominant detection signature. We describe the regimes below at the level of physical mechanism and detection signature; quantitative case studies are deferred to Sec. VII.

*a. Regime I – Continuum-disguised AGN-class events.* A subset of AGN-related transients (Blazars, BL Lac objects, some QSOs) have featureless blue continua that overlap with the accretion continua of cataclysmic variables in the wavelength range accessible to low-resolution rapid spectrographs. Closed-set classifiers map these spectra confidently to the CV class – in our test sample, 10/11 Blazars are mis-classified as CVs with mean confidence  $\hat{p}_{\text{CV}} = 0.79$ . The softmax probability is uninformative for these spectra (entropy low, MSP<sup>2</sup> high), and within-class typicality is also uninformative because the embedding is mapped near a CV centroid. Density-based scores produce only a moderate signal. *No single family-only mini-ensemble fires at the 1% false-alarm rate on these spectra.* Detection is carried entirely by the cross-family non-linear combiner, which integrates a weak signal from each family into a saturation-level anomaly score. This regime is the strongest empirical case for cross-family combination.

*b. Regime II – Spectroscopic disguise within physical neighbours.* A second regime arises from genuine spectroscopic similarity between a rare class and a training class. The clearest examples are calcium-rich transients – whose strong Ca II features and stripped-envelope continua are spectroscopically near-degenerate with SNe Ib/c – and classical/recurrent novae, whose Balmer-dominated emission spectra resemble certain CV outbursts. In our test set *all* 10 Ca-rich transients are classified as Ib/c or II, and only 1 is flagged by any family-only mini-ensemble at the 1% false-alarm rate; the full cross-family pipeline recovers 4/10. For novae the same pattern holds at population scale: only 4/67 are caught by any family alone, while the full pipeline catches 54/67. Like Regime I, this regime is recovered only by cross-family combination; unlike Regime I, the dominant signature is within-class distance (the embedding sits in the tail of its predicted-class distribution) rather than projection-space disagreement.

*c. Regime III – Continuum-dominated mis-classifications.* Some rare classes – GRB afterglows in particular – produce featureless or weak-feature spectra that the classifier maps to training classes (typically CV, occasionally SLSN<sup>3</sup>) with intermediate confidence ( $\hat{p} \sim 0.5$ – $0.85$ ). Unlike Regime I, the embedding of these spectra is genuinely far from the predicted-class centroid: within-class Mahalanobis is in the extreme tail, GMM negative log-density is high, and *both* the distance and density family ensembles fire independently. All 17 afterglows in our rare set are recovered. This is the regime where embedding-based scores fundamentally outperform softmax-based ones, and where a single sufficiently-discriminative family-only score (global or within-class Mahalanobis) would already perform well.

<sup>2</sup>MSP: maximum softmax probability

<sup>3</sup>SLSN: Super Luminous Supernova (SN).

*d. Regime IV – Legitimately ambiguous progenitor regimes.* Some rare classes are genuinely intermediate between multiple physical channels: FBOTs have been variously attributed to engine-driven explosions, failed supernovae, and Intermediate Massive Black Hole (IMBH) tidal disruption events [11, 12, 30, 31]; ILRTs have been variously attributed to electron-capture supernovae and non-terminal eruptions [13, 32]. In our test sample, FBOT predictions scatter across CV, TDE, Ia, II, and Ibc labels with confidence ranging from 0.30 to 0.89 and family-vote counts spanning the entire 0–4 range; ILRTs scatter similarly across H-rich core-collapse subclasses. The classifier here is *correctly* uncertain; the cross-family ensemble integrates moderate signals from multiple families into reliable detection (90/98 FBOTs and 27/33 ILRTs caught by the framework). This regime is the survey-operations bread-and-butter for the framework.

*e. Regime V – Far-out-of-distribution events.* At the extreme end are events that do not resemble any training class at the manifold level; the long GRB AT2022cva [33, 34] in our test set is the textbook example. All four families fire with strong signal, multiple voting methods agree, and any reasonable single-metric detector would already flag the event. These are the easy cases for any anomaly detection framework; they are included to anchor the expected behaviour and to provide a per-class point of reference.

*f. Design implication.* The five regimes have different detection signatures and therefore require different mathematical machinery for recovery. Regimes I and II are recoverable only through cross-family non-linear combination; Regimes III and IV are recoverable by embedding-based scores and benefit from corroboration across families; Regime V is recoverable by any sufficiently sensitive score. The upper bound on a single-family pipeline is therefore set by Regimes I and II, which together comprise a substantial fraction of the rare-anomaly population (the AGN-related sub-population and the novae+Ca-rich sub-population together,  $\sim 43\%$  of the rare set). The cross-family non-linear combiner we develop in Sec. IV is the smallest machinery that unifies all five regimes.

### III. DATASET

Spectroscopic data ingestion is handled by IRIS (Identification and Reduction of Interesting Spectra), the data-side module of the ASTRANet framework. IRIS provides an end-to-end preprocessing pipeline that (i) fetches spectroscopic candidates from the Fritz/SkyPortal marshal [35, 36] via the GraphQL API, (ii) cross-matches candidates with the Transient Name Server (TNS) classification, (iii) applies a unified quality-control filter (SNR threshold, wavelength coverage  $\geq 80\%$  of the [3850, 9000] Å window, flatness rejection, and removal of variable-star, bogus, or multi-label objects),

(iv) maps raw TNS classifications to the fine and coarse taxonomies (Table XIV), (v) partitions the cleaned set at the object level into training, rare-anomaly, and out-of-distribution evaluation subsets, and (vi) builds uniform-grid PyTorch tensors ready for inference. The IRIS pipeline is released as an open-source package [37].

The dataset used in this work is the output of IRIS applied to the ZTF spectroscopic follow-up campaign [38–40]. The bulk of the spectra come from the SED Machine [SEDM; 8, 41, 42], the low-resolution spectrograph dedicated to ZTF transient classification, supplemented by Keck [43, 44], Gemini [45], the LBT [46], and the Next Generation Palomar Spectrograph [NGPS; 47], the new P200 instrument for ZTF/BTS transient classification. Beyond this core, an international network of instruments contributes to transient classification – for example SDSS [48], DESI [49] – and we refer the reader to Junell *et al.* [28] for a more comprehensive list. Follow-up triggering and data management are supported by dedicated software infrastructure: the SkyPortal [35, 36], Fritz<sup>4</sup>, and GROWTH [50] marshals together with the Transient Name Server<sup>5</sup> (TNS), with alternative platforms such as YSE-PZ [51].

Splits are made at the object level (70%/15%/15%, train/val/test): all spectra of a given object fall in the same subset, so no object’s spectra leak across the split boundary regardless of how many epochs it has. Separately, because spectra are aggregated from partially overlapping sources – the same observation can be present in both the Fritz/SkyPortal and GROWTH marshals, or reported to TNS and the local marshal independently – a small number of numerically identical spectra appear in the raw set. These would double-count the affected objects in training and in the reported metrics, so IRIS removes any pair of flux vectors agreeing to within  $\epsilon < 10^{-6}$ . Objects without confident classifications ( $p_{\text{TNS}} < 0.5$ ) are also excluded.

*a. Taxonomy.* Raw TNS classifications include  $\geq 23$  subtypes, many spectroscopically inseparable at SEDM resolution and several with  $< 100$  examples in our database. We merge these into  $K_f = 7$  head classes used by the fine head of the network: SN Ia, SN Ibc (Ib  $\cup$  Ic  $\cup$  Ibc  $\cup$  Ibn), SLSN, SN II (II  $\cup$  II<sub>n</sub>  $\cup$  II<sub>b</sub>), AGN, CV, and TDE. The coarse head groups these into three superclasses: SN-Thermonuclear ({Ia}), SN-CC<sup>6</sup> ({Ibc, II, SLSN}), and Non-SN ({AGN, CV, TDE}). The full mapping and per-class training counts appear in Table XIV; rationale and the complete raw-subtype distribution are in the Appendix D. The SN Ia class explicitly includes the full peculiar-thermonuclear family (Ia-91T, Ia-91bg, Ia-02cx/Iax, Ia-03fg, Ia-CSM, Ia-pec; 478 spectra across the three splits). Keeping the peculiar subtypes inside SN Ia rather than discarding them is a deliberate choice:

<sup>4</sup><https://github.com/fritz-marshall/fritz>

<sup>5</sup><https://www.wis-tns.org/>

<sup>6</sup>CC: Core Collapse

it forces the classifier to learn the intrinsic diversity of the thermonuclear class, and it reserves the anomaly-detection layer for objects that are genuinely outside the training taxonomy rather than for known subtypes of a common class.

*b. Out-of-distribution evaluation set.* We assemble a held-out rare-anomaly evaluation set of  $N = 289$  spectra across 11 classes deliberately excluded from training (Table XIV, lower block). The set is constructed to span the five failure-mode regimes of Sec. II rather than to maximise sample size: AGN outliers (QSO, Blazar, BL Lac) anchor Regime I; calcium-rich supernovae together with classical and recurrent novae anchor Regime II; GRB afterglows anchor Regime III; gap transients (ILRT, FBOT) anchor Regime IV; long GRBs and luminous red novae anchor Regime V. We deliberately retain physical ambiguity in ILRTs and FBOTs – forcing them into existing categories would obscure genuine astrophysical uncertainty about their progenitors [10–13, 30–32].

*c. Preprocessing.* Each spectrum is restricted to the *observer-frame* wavelength interval  $[3850, 9000] \text{ \AA}$  and linearly interpolated onto a uniform grid of  $L = 4096$ . No rest-framing and no continuum removal are applied at any stage of the pipeline: host-galaxy redshift is provided to **ASTRANet** as optional metadata (Sec. IV A) and is randomly masked during training so the network learns redshift-invariant spectral representations, while the full continuum shape is retained as discriminative information for continuum-dominated classes (AGN, TDE, SLSN). The interpolated flux is then scaled per spectrum with a robust percentile transform  $f \mapsto (f - p_5)/(p_{95} - p_5)$ , which compresses outlier emission/absorption excursions without zeroing the local dynamic range. Missing flux values are zero-filled with a validity mask. A second input channel carries a Savitzky–Golay first derivative (window 7, order 3) computed after augmentation, highlighting narrow features. Full preprocessing details are in Appendix D 0 a.

#### IV. THE ASTRANET FRAMEWORK

The **ASTRANet** framework integrates data ingestion, classification, anomaly detection, and uncertainty quantification into an end-to-end pipeline. The four named modules are:

- **IRIS** (Sec. III): the data-ingestion module that fetches candidates from the **Fritz**/SkyPortal marshal, applies quality-control filtering, maps to the FINE\_10/COARSE\_6 taxonomies, and outputs uniform-grid PyTorch tensors [37].
- **ASTRANet** (Sec. IV A): the hierarchical deep ensemble classifier that takes an SEDM-resolution spectrum as input and produces an embedding  $\mathbf{e} \in \mathbb{R}^{192}$ , fine-class softmax  $\hat{p}(y | x)$  over  $K_f = 7$  classes, and coarse-class softmax over  $K_c = 3$  superclasses.
- **ASTRANet-Sentinel** (Sec. IV D): the anomaly detection layer. Sixteen complementary scores computed on the **ASTRANet** embedding (Mahalanobis, kNN distance, GMM density, isolation forest, cosine deviation, hierarchical-energy mismatch, and ten others; Appendix C) are non-linearly combined into a single cross-family AD score  $s_{\text{AD}}(x) \in [0, 1]$ .
- **ASTRANet-CP** (Sec. VI): the conformal uncertainty quantification layer. Mondrian conformal prediction calibrates  $s_{\text{AD}}$  into a per-spectrum p-value  $p_M$ ; adaptive prediction sets provide coverage at user-specified  $\alpha$ ; per-class ensemble probability intervals  $\{\bar{p}_k \pm \sigma_k\}$  summarise the deep-ensemble disagreement; and AD-stratified Mondrian CP (AD-MCP, Sec. VI H) achieves uniform conditional coverage across anomaly-score strata.

The present section describes the three ML-side modules at the design level. Architectural details, loss-function specifics, and training hyperparameters are deferred to Appendices A–B; the explicit definitions of the 16 anomaly scores are in Appendix C.

##### A. The ASTRANet classifier

**ASTRANet** is a hierarchical spectral classifier (Fig. 1) that jointly predicts coarse superclass and fine-grained type. The hierarchical structure is motivated by the underlying physics: the coarse partition (thermonuclear vs. core-collapse vs. non-SN) reflects distinct progenitor channels with substantially disjoint spectral signatures, while the fine partition resolves sub-classes that share a physical channel. Each input spectrum is represented as a two-channel signal of length  $L = 4096$ : the robust-scaled flux (Sec. III, with continuum shape retained) and its Savitzky–Golay first derivative, which highlights narrow line features without amplifying noise.

The architecture has four functional blocks:

- a *multi-scale convolutional stem* with parallel kernels  $k \in \{7, 31, 151\}$ , designed to operate at the three native scales of supernova spectra: narrow emission/absorption lines, broad P-Cygni features, and continuum shape.
- a *dilated temporal convolutional backbone* [52] with six residual blocks and exponentially increasing dilation, reaching a  $\sim 250$ -sample receptive field;
- *metadata conditioning via Feature-wise Linear Modulation* [FiLM; 25], injecting spectral phase, host redshift, and instrument identifier as *optional* metadata at two points. Each metadata channel carries a validity bit and is randomly masked during training so the network learns to classify, detect anomalies, and quantify uncertainty under partial or fully missing metadata;

- *hierarchical classification heads* producing a 3-way coarse superclass prediction (SN-Thermonuclear / SN-CC / Non-SN) and a 7-way fine prediction (Ia / Ibc / SLSN / II / AGN / CV / TDE), with stop-gradient between them so the fine head consumes the coarse softmax as a soft prior without back-propagating into the coarse representation. We note that this progenitor-based partition does not always coincide with spectroscopic similarity at a given epoch: at photospheric phases, e.g., SN Ib can resemble SN Ia more than Type II, which the fine head must resolve and which contributes to the residual Ibc/II/Ia confusion structure of Fig. 2.

Multi-head attention pooling [53] aggregates the backbone output into a 192-dimensional embedding  $\mathbf{e}$ ; separate  $\ell_2$ -normalised projection heads supply the supervised contrastive loss [54] that shapes the embedding geometry the AD layer depends on (Sec. IV D). The training objective combines focal loss [55] on the fine head, cross-entropy on the coarse head, supervised-contrastive terms at both granularities, a targeted confusion penalty that suppresses physically harmful misclassifications (TDE $\rightarrow$ Ia, II $\rightarrow$ Ibc, SLSN $\rightarrow$ Ibc), and an attention-entropy bonus that prevents the model from collapsing onto a single spectral region. The model is trained with AdamW [56] under cosine warm restarts, balanced sampling, MixUp [57], and effective-number class re-weighting [58], with EMA-tracked weights for inference. Full hyperparameters and per-component design choices appear in Appendix A, with the loss weights in Table XI.

## B. Deep-ensemble backbone

A single ASTRANet model produces point estimates of the embedding and softmax probabilities. To reduce sensitivity to initialisation and to supply implicit uncertainty quantification [59], we construct an ensemble of  $M = 6$  checkpoints obtained from three independent random seeds across two architecture revisions. For each spectrum we compute per-model embeddings  $\mathbf{e}^{(m)}$  and softmax probabilities  $\mathbf{p}^{(m)}$ , average them within each seed, and then across seeds, yielding  $(\bar{\mathbf{e}}, \bar{\mathbf{p}})$ . We verified that this two-stage scheme outperforms both a flat super-ensemble and a cross-seed-only average; eight ensembling strategies are systematically benchmarked in Appendix G. The ensemble averages feed all downstream anomaly-detection scores and the uncertainty-quantification layer; the per-model softmaxes additionally supply the per-class ensemble intervals  $\{\bar{p}_k \pm \sigma_k\}$  reported by ASTRANet-CP.

## C. Sixteen complementary anomaly scores

The anomaly-detection layer computes 16 scores from the ensemble embeddings and logits, spanning four phys-

ically motivated families. Each family captures a qualitatively different way in which a spectrum can be “unusual” and maps onto a different subset of the failure-mode regimes of Sec. II:

**Uncertainty (4 scores):** maximum softmax probability [18], predictive entropy, ODIN [60], and energy [61]. These quantify how confident the classifier is at the logit level and are the natural detectors for Regimes IV–V, where the classifier itself signals uncertainty.

**Distance (6 scores):** global, class-conditional, and within-predicted-class Mahalanobis distances [62];  $k$ -nearest-neighbour distance; cosine distance to the nearest class projection centroid; and a class-conditional typicality. These quantify how far the spectrum lies from the manifold of in-distribution embeddings and target Regimes II–III, where the classifier’s confidence is uninformative but the embedding is anomalous.

**Density (4 scores):** per-class Gaussian-mixture likelihoods, isolation forest [63], local outlier factor [64], and PCA-reconstruction error. These quantify how sparse the embedding’s local neighbourhood is and complement the distance family at Regime III.

**Hybrid (2 scores):** a hierarchical entropy combination (HEC) mixing fine-head entropy, coarse-head entropy, and parent-child inconsistency; and a per-class manifold residual score (MRS) computed against per-class PCA subspaces. These exploit the hierarchical architecture explicitly and target Regime IV (legitimate progenitor ambiguity that manifests as parent/child label disagreement).

Regime I – continuum-disguised AGN-class events – is the failure mode for which *no single family is sufficient*, since the classifier is confident, the embedding is mapped near an in-distribution centroid, and the density signal is only moderate. This is the regime that motivates the non-linear cross-family combiner introduced next. All scores adopt the convention *higher = more anomalous*; each is rank-normalised against the in-distribution validation pool before being combined. Mathematical definitions, justifications, and individual benchmarks appear in Appendix C.

## D. The ASTRANet-Sentinel anomaly detection layer

The ASTRANet-Sentinel module combines the 16 rank-normalised scores via a gradient-boosted decision-tree model [LightGBM; 65] trained with 5-fold cross-validation on the validation set, producing a single cross-family anomaly score  $s_{\text{AD}}(x) \equiv s_{\text{ensemble}}(x) \in [0, 1]$ . The non-linearity is essential: as we show in Sec. V C, the majority of detections come from spectra whose anomaly

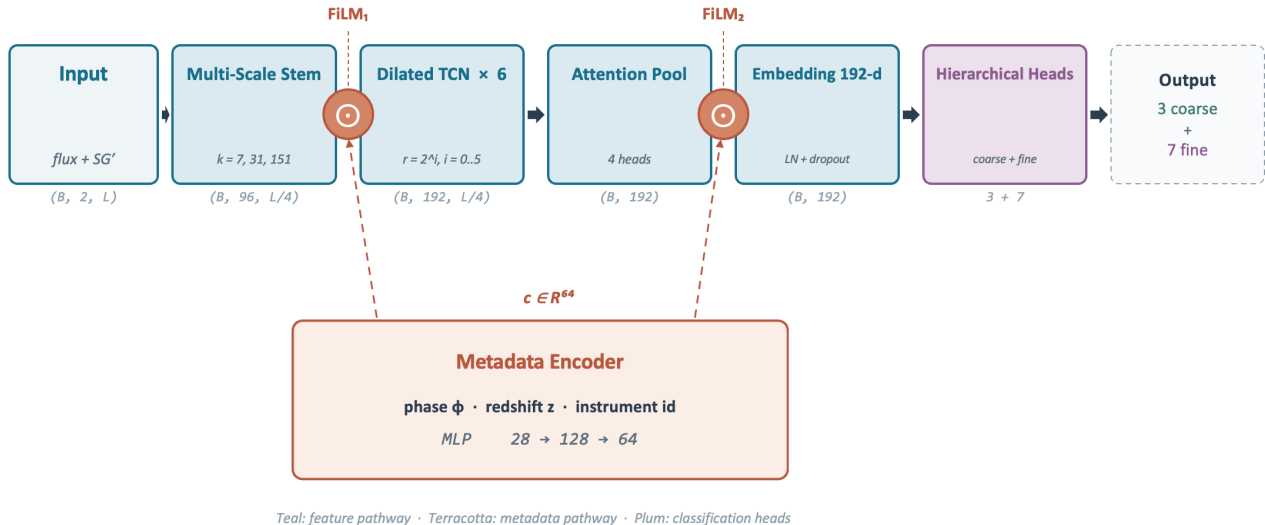


FIG. 1. Architecture of **ASTRANet**. Spectral features are extracted by a multi-scale stem and a dilated TCN backbone, fused with observational metadata via FiLM conditioning, aggregated by multi-head attention pooling, and passed to hierarchical coarse/fine classification heads. The 192-dimensional embedding  $\mathbf{e}$  supplies the anomaly-detection layer (Sec. IV D); separate projection heads supply the contrastive loss. Detailed sub-figures and dimensions are in Appendix A.

signals are individually below threshold in *every* family and only become detectable through cross-family interaction. We benchmarked three linear baselines (an AUROC-weighted rank average, a decorrelated logistic regression, and a full 16-feature logistic regression); all are substantially outperformed by the gradient-boosted combiner. Comparison numbers and feature-importance breakdown appear in Sec. VB and Appendix C.

*a. Operating points.* The same  $s_{AD}$  supports three operating regimes for survey-mode triage: (i) a single *anchor threshold* on the seed-averaged score at a fixed false-alarm rate; (ii) *per-seed detectors* thresholded independently; and (iii) a *seed-union* that flags any sample caught by at least one seed, trading false-alarm budget for recall. The choice between regimes is exposed to the user as a single  $\alpha$  parameter in the conformal extension (Sec. VI), recovering all four as special cases. Empirical operating-point analysis is in Sec. VD.

*b. Outlier-exposure fine-tuning.* Before scoring, the encoder is fine-tuned with an outlier-exposure objective [66]: the classification loss on the training set is augmented with (i) an entropy term that pushes exposure anomalies toward a uniform softmax and (ii) an embedding-margin term that pushes their embeddings at least a margin away from every class centroid ( $\lambda_{OE} = \lambda_{emb} = 1$ , 20 epochs). Exposure anomalies are always drawn from folds disjoint from those being evaluated (Sec. VD), so no detected object ever contributed to its own detector. This step is what closes the near-OOD gap: it raises leakage-free recovery at 1% FAR from 34.3% to 82.4% of rare spectra, with the largest gains exactly in the spectroscopic-disguise regime (novae, ILRTs; Sec. VE).

*c. Inference cost.* For each new spectrum the pipeline performs  $M = 6$  forward passes through the **ASTRANet** ensemble, averages embeddings and logits, computes the 16 scores from the averaged tensors, rank-normalises them against pre-computed validation distributions, and feeds them to the LightGBM combiner. Total cost is  $< 200$  ms per spectrum on a single GPU, dominated by the deep-ensemble forward passes; the out-of-distribution (OOD) scoring layer adds  $< 50$  ms on CPU. The full pipeline is below the per-spectrum cadence of any current or planned spectroscopic time-domain survey.

## V. VALIDATION

### A. Classification performance

**ASTRANet** achieves 87% overall accuracy and 83% macro recall on the held-out test set ( $N = 3,396$  spectra, of which 82 are peculiar-Ia) using the within-seed checkpoint ensemble, our default deployment configuration. Per-class recalls range from 77% (TDE) to 93% (SN Ia); the remaining classes are SN Ibc (78%, the hardest CC subclass), AGN (78%, the hardest non-SN class due to blue continua at intermediate phases), SN II (80%, confused mainly with SN Ibc), CV (87%), and SLSN (88%). Appendix E compares this methodology with other baselines. Eight ensembling strategies are systematically compared in Appendix G; none of four advanced learned strategies consistently improves over within-seed averaging, indicating that residual errors are driven by intrinsic spectral overlap rather than ensemble

True label \ Predicted label	Ia	Ibc	SLSN	II	AGN	CV	TDE
Ia	93% (1656)	3% (54)	0% (3)	3% (55)	0% (4)	1% (9)	
Ibc	7% (32)	78% (332)	3% (14)	10% (44)	0% (1)	1% (4)	0% (1)
SLSN	4% (1)	4% (1)	88% (22)				4% (1)
II	5% (44)	10% (93)	1% (8)	80% (755)	2% (15)	1% (10)	2% (23)
AGN	11% (5)		2% (1)	2% (1)	78% (35)	7% (3)	
CV			1% (1)	8% (10)	4% (5)	87% (106)	
TDE	15% (7)	2% (1)		2% (1)	2% (1)	2% (1)	77% (36)

FIG. 2. Confusion matrix on the held-out test set ( $N=3,396$  spectra) using the within-seed checkpoint ensemble. Entries are row-normalised to per-class recall (%). Off-diagonal mass concentrates on physically expected confusions (Ibc/II, AGN/TDE).

sub-optimality.

## B. OOD detection: metric comparison

We evaluate AUROC and AUPRC for all 16 individual OOD scores and the four ensemble strategies on the rare-anomaly evaluation set ( $N=289$  rare/peculiar/out-of-taxonomy transients vs. a held-out validation pool of 3,339 in-distribution samples), with 95% bootstrap confidence intervals over 2000 resamples. Full numerical breakdown of all 16 scores and four ensembles is in Table XIII (Appendix C).

The top seven individual methods are all embedding- or projection-based, while all four logit-based uncertainty methods and the HEC hybrid cluster below AUROC 0.755. This gap is the empirical signature of the failure-mode taxonomy of Sec. II: softmax-based scores are blind to spectra that the classifier confidently mis-classifies (Regimes I–III), while embedding-based scores recognise that those spectra lie far from the in-distribution manifold. The LightGBM ensemble reaches 0.996 test AUROC; linear logistic regression on all 16 scores already reaches 0.9760 but cannot match the non-linear combiner, whose advantage we trace to cross-family interactions in Sec. V C.

## C. Why a single score family is not enough

The systematic gain from combining the 16 scores comes not from averaging redundant signals but from genuine complementarity between the four score families. To show this, we built four “family-only” mini-ensembles by mean-rank averaging the rank-normalised scores within each family and thresholded each at the same 1% validation false-alarm rate as the full LightGBM ensemble.

Table I shows the resulting per-family AUROCs and detection counts. *No single family approaches the full pipeline*: the strongest family-only detector (distance, AUROC = 0.8823) recovers only 86/289 rare spectra at 1% FAR; the density family is close behind (80/289); hybrid and uncertainty trail at 26/289 and 22/289 respectively. Under the leakage-free  $k$ -fold protocol of Sec. V D, the base LightGBM combination of all 16 scores recovers 99/289 (34.3%) at 1% FAR; adding outlier-exposure fine-tuning of the encoder (Sec. IV D) lifts this to 238/289 (82.4%) at the same FAR, and to 244/289 (84.4%; 80.4% of unique objects) under the seed-union strategy at an effective  $\sim 3\%$  FAR.

*a. Per-anomaly complementarity.* At the 1%-FAR operating point, 106 of the 289 rare anomalies are caught by at least one family-only mini-ensemble (28 by exactly one family, 55 by two, 16 by three, 7 by all four); the remaining 183 are caught by *no* family alone. The outlier-exposed **Sentinel** flags 238 samples, of which 137 (57.6%) *come from anomalies no family-only ensemble catches* – the near-OOD classes dominate this set (no-vae alone jump from 4/67 caught by any single family to 54/67 under the full pipeline, the largest absolute gain). This is the empirical content of the Regime I/II argument of Sec. II: near-OOD events whose individual family signals are weak are recoverable only by an ensemble that integrates evidence across families non-linearly. Figure 3 shows the per-spectrum detection map.

## D. Detection strategies and operating points

A key practical strength of the framework is that survey teams can choose the detection regime appropriate for their use case. All operating points below are evaluated under a *leakage-free* protocol: the 289 rare spectra are split into  $k=5$  stratified folds; for each fold the encoder is fine-tuned with outlier exposure on the *other* four folds (Sec. IV D), the LightGBM combiner is trained on half of the validation pool plus the exposure folds, the detection threshold is set at a 1% false-alarm rate on the *held-out* half of the validation pool, and detections are counted only on the held-out fold. No rare spectrum is ever seen – in fine-tuning, combiner training, or thresholding – by the detector that scores it. The procedure is repeated for three independently trained seeds.

*a. Anchor (score-averaged ensemble).* Averaging the three seeds’ **Sentinel** scores and thresholding

TABLE I. Per-family OOD detection performance on the  $N=289$  rare set. Family ensembles built by averaging rank-normalised scores within each family; thresholds set at the same 1% validation false-alarm rate as the full LightGBM combiner.

Family	AUROC	Det at 1% FAR	Det %
Uncertainty (4 scores)	0.7184	22/289	7.6%
Hybrid (2 scores)	0.7957	26/289	9.0%
Density (4 scores)	0.8809	80/289	27.7%
Distance (6 scores)	0.8823	86/289	29.8%
LightGBM (all 16, 5-fold CV)	$0.947 \pm 0.016$	99/289	34.3%
+ <b>outlier exposure (3-seed)</b>	–	<b>238/289</b>	<b>82.4%</b>

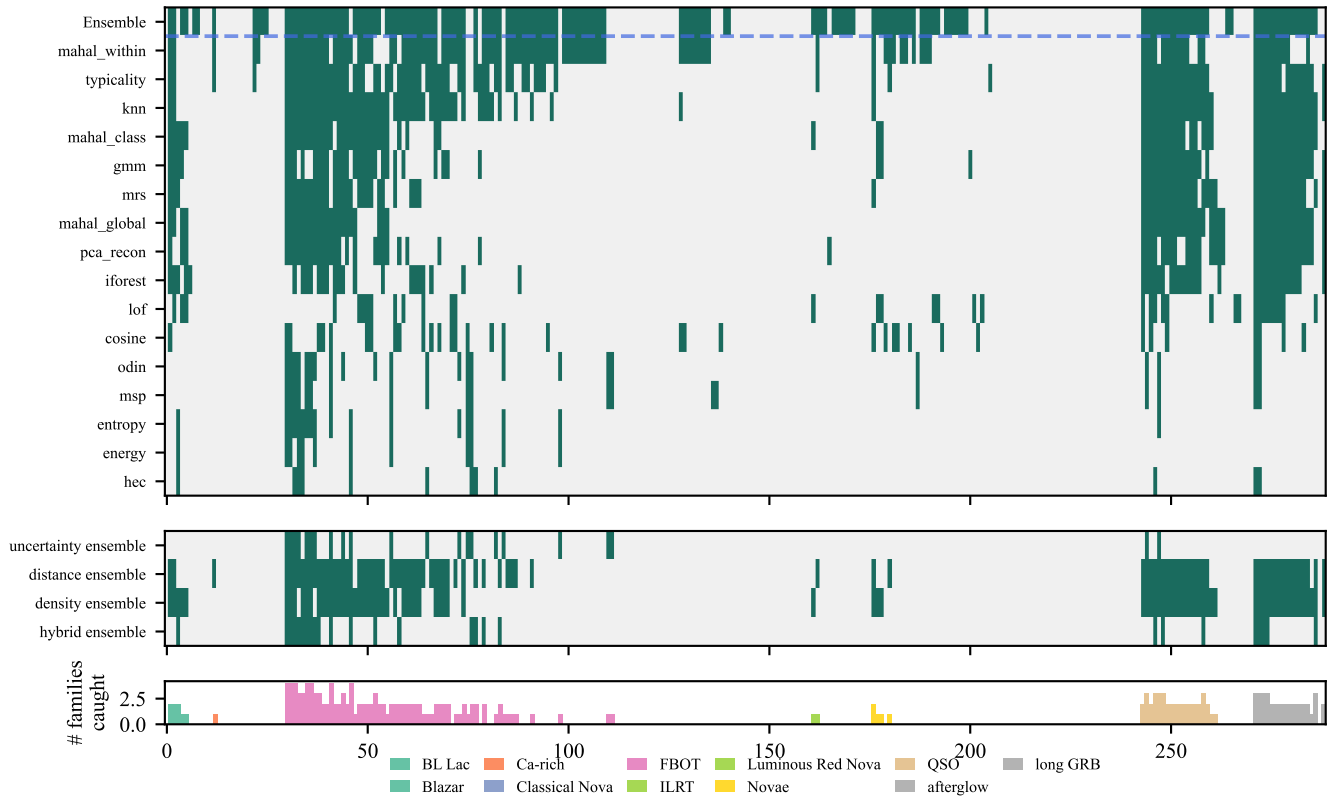


FIG. 3. Per-anomaly detection map at 1% false-alarm rate. Each column is a rare spectrum, sorted by true class and then by the number of families that flag it. *Top row*: the LightGBM ensemble of all 16 scores. *Middle block*: the 16 individual OOD scores, sorted by individual AUROC and annotated with their family. *Lower block*: the four family-only mini-ensembles. *Bottom panel*: number of families that catch each anomaly, coloured by true class. Ca-rich, Classical Nova, Novae, and ILRT contain large numbers of spectra the LightGBM ensemble flags but no family alone recovers.

at the (averaged) 1%-FAR anchor recovers 238/289 spectra (82.4%), corresponding to 81/107 unique objects (75.7%).

*b. Per-seed detectors.* Individual seeds recover  $75.1 \pm 0.7\%$  of spectra ( $68.2 \pm 1.5\%$  of objects) at their own 1%-FAR thresholds – the seed-to-seed scatter is small, and the ensemble anchor adds  $\sim 7$  points over any single seed.

*c. Seed-union.* Flagging a spectrum caught by any of the three seeds trades false-alarm budget for recall: 244/289 spectra (84.4%) and 86/107 objects (80.4%) at an effective  $\sim 3\%$  in-distribution false-positive rate. This is the natural survey-mode triage point.

*d. Choice of operating regime.* We recommend: *survey-mode triage* (high recall, moderate FP cost) – the seed-union (84.4% of spectra, 80.4% of objects, at  $\sim 3\%$  FP); *high-purity follow-up* (every flagged spectrum likely receives telescope time) – the score-averaged anchor at 1% FAR (82.4% recall); *pure ranking* (priority queue for human scanners) – the averaged **Sentinel** score directly, with no threshold.

TABLE II. Comparison of detection strategies on the rare-anomaly evaluation set ( $N = 289$  spectra, 107 objects) under the leakage-free  $k$ -fold protocol. “Missed” counts rare spectra not flagged.

Strategy	Rare det. (spectra)	Rare det. (objects)	Eff. FAR	Missed
Base combiner, no OE (3-seed avg.)	34.3%	–	1.0%	190
Per-seed OE (mean $\pm$ std)	$75.1 \pm 0.7\%$	$68.2 \pm 1.5\%$	1.0%	$\sim 72$
<b>Anchor: 3-seed score average</b>	<b>82.4%</b>	<b>75.7%</b>	<b>1.0%</b>	<b>51</b>
Seed-union	84.4%	80.4%	$\sim 3\%$	45

### E. Per-class detection difficulty

The recovery hierarchy aligns with astrophysical expectations, and we report it in two tiers that separate what a detection *means*. **Tier 1 – genuinely novel phenomena** (no trained counterpart class): the score-averaged anchor recovers 27/35 objects (77%), rising to 28/35 (80%) under the seed-union. Within this tier, FBOTs (92/98 spectra, 94%), GRB afterglows (16/17, 94%), the long GRB (1/1), luminous red novae (13/15, 87%) and ILRTs (27/33, 82%) are reliably flagged; Ca-rich transients (4/10 spectra, 2/5 objects) remain the hardest class, mapped almost uniformly to SN Ib/c – their strong Ca II features and stripped-envelope continua are spectroscopically near-degenerate with the training class. **Tier 2 – rare members of trained families**, where reduced sensitivity is partly *correct* behaviour: classical and recurrent novae are cataclysmic variables in eruption and live inside the trained CV manifold, yet outlier exposure recovers 54/67 nova spectra (81%) and 5/8 classical novae; the AGN-family outliers (QSO 20/28 spectra, Blazar 5/11, BL Lac 0/1) sit inside the trained AGN manifold and are flagged at correspondingly lower rates. Overall the anchor recovers 75% of Tier-2 objects and 77% of Tier-1 objects, and the seed-union 81% and 80% respectively. This hierarchy provides practical guidance for survey operations: the pipeline reliably flags genuinely novel phenomena (afterglows, GRBs, fast transients, LRNe, ILRTs) while near-degenerate gap transients (Ca-rich) need additional follow-up data (light-curve evolution, host-galaxy properties) to be distinguished from genuine stripped-envelope supernovae.

*a. Case-study anchor.* Concrete per-spectrum examples spanning these regimes – including the Regime-B cases (Blazar AT 2024uln, FBOT AT 2024wpp) where the model is confident on a wrong class, at most one family-only ensemble fires, yet  $s_{\text{ens}} \geq 0.93$  – are presented with full astrophysical interpretation in Sec. VII (Table X).

## VI. THE ASTRANET-CP CONFORMAL UNCERTAINTY LAYER

Anomaly detection (ASTRANet-Sentinel, Sec. IV D) and classification (Sec. V A) are usually presented as distinct outputs. In survey-mode triage they are insepa-

TABLE III. Per-class detection statistics on the rare set ( $N = 289$ ) under the leakage-free  $k$ -fold protocol. “Det.” is the number of spectra flagged by the seed-averaged Sentinel at the 1%-FAR anchor (threshold 0.087); “Det. %” is per-class recall; “Ens. score” is the mean seed-averaged combiner score across spectra of that class (scores are held-out  $k$ -fold probabilities and are not calibrated toward 1).

Class	$N$	Detected	Det. %	Ens. score
long GRB	1	1	100.0%	0.374
afterglow	17	16	94.1%	0.899
FBOT	98	92	93.9%	0.833
Luminous Red Nova	15	13	86.7%	0.829
ILRT	33	27	81.8%	0.514
Novae	67	54	80.6%	0.680
Classical Nova	8	6	75.0%	0.601
QSO	28	20	71.4%	0.518
Blazar	11	5	45.5%	0.364
Ca-rich	10	4	40.0%	0.258
BL Lac	1	0	0.0%	0.003

table: a spectrum flagged as anomalous still requires a per-class probability to decide how to allocate follow-up resources, and a confident classification still requires a calibrated tail probability to decide whether the confidence can be trusted. We introduce ASTRANet-CP, the conformal uncertainty layer that extends the 16-score AD framework of Sec. IV D to *distribution-free* uncertainty quantification via Mondrian conformal prediction [67, 68]. The framework produces, for every spectrum: (i) a calibrated conformal p-value of the LightGBM anomaly score; (ii) an adaptive prediction set  $\mathcal{C}_\alpha(x)$  of plausible classes at user-specified coverage  $1 - \alpha$  [69]; (iii) a decomposition of predictive entropy into aleatoric and epistemic components using the deep ensemble’s per-model variance.

*a. Calibration setup.* We split the in-distribution validation pool (3,339 spectra) randomly into a calibration set ( $n_{\text{cal}} = 1,669$ ) and a held-out exchangeability-test set ( $n_{\text{ho}} = 1,670$ ). To avoid leakage of training information into calibration, the LightGBM anomaly scores used by the conformal procedure are produced by 5-fold out-of-fold prediction on the union of validation and rare spectra; this yields an OOF AUROC of 0.9983 on the rare set, in line with the cross-validated estimate of Sec. IV D. (These OOF scores serve calibration analysis only; detection headlines use the leakage-free protocol of Sec. V D.)

TABLE IV. Conformal calibration and OOD detection at four canonical  $\alpha$  values. “Marg. cov.” and “Mond. cov.” are empirical in-distribution coverage of the marginal and Mondrian predictors (target  $1 - \alpha$ ); “Mond. det.” is the rare-set detection rate at the Mondrian operating point ( $p_M < \alpha$ ).

$\alpha$	Target cov.	Marg. cov.	Mond. cov.	Mond. det.
0.010	0.990	0.987	0.986	29.8%
0.025	0.975	0.972	0.966	38.1%
0.050	0.950	0.949	0.940	89.6%
0.100	0.900	0.888	0.886	99.7%

### A. Conformal calibration of the AD score

Given a calibration set  $\{(x_i, y_i)\}_{i=1}^n$  and a nonconformity score  $s(x, y)$  (higher = more atypical), the conformal p-value of a new point  $x^*$  with predicted class  $\hat{y}$  is

$$p(x^*) = \frac{|\{i : s(x_i, y_i) \geq s(x^*, \hat{y})\}| + 1}{n + 1}. \quad (1)$$

We adopt the LightGBM ensemble score as the nonconformity function. Eq. 1 gives *marginal* coverage; the *Mondrian* variant partitions the calibration set by predicted class and applies Eq. 1 within each partition, providing per-class FDR control [67, 68]:

$$p_M(x^*) = \frac{|\{i : \hat{y}_i = \hat{y}(x^*) \wedge s_i \geq s(x^*)\}| + 1}{|\{i : \hat{y}_i = \hat{y}(x^*)\}| + 1}. \quad (2)$$

*a. Empirical coverage.* Empirical coverage tracks the nominal level almost exactly across  $1 - \alpha \in [0.80, 0.995]$  (Table IV): at  $\alpha = 0.05$  the marginal procedure achieves 0.949 empirical coverage against 0.950 nominal, and Mondrian achieves 0.940. The curves sit on the diagonal within the expected  $\pm 0.5 n_{\text{ho}}^{-1/2} \approx \pm 0.012$  finite-sample error, confirming the LightGBM-OOF score satisfies the exchangeability assumption conformal prediction requires. Figure 4 shows the resulting p-value distributions: the ID distribution is statistically indistinguishable from uniform while the OOD distribution piles near zero.

*b. OOD detection at calibrated alpha.* Table IV summarises the rare-set detection rate at four canonical  $\alpha$  values. At  $\alpha = 0.10$  (the natural high-recall operating point) the Mondrian predictor recovers 99.7% of the rare anomalies. This sequence is mathematically equivalent to a LightGBM threshold sweep on the OOF scores; the  $\alpha = 0.01$  Mondrian operating point corresponds to the OOF anchor threshold as a special case. The advantage of the conformal formulation is interpretive: a Mondrian p-value of 0.04 for a CV-predicted spectrum means “among in-distribution CV-class calibration spectra, only 4% are at least this anomalous”.

*c. Per-class coverage.* At  $\alpha = 0.025$ , five of seven predicted classes achieve coverage within  $\pm 2\%$  of the 0.975 target (Table V); the exceptions are TDE (0.787) and CV (0.917), reflecting their small calibration samples ( $n_{\text{cal}} = 42$  and 60) and the expected finite-sample

TABLE V. Mondrian conformal per-class diagnostics at  $\alpha = 0.025$ . “ $n_{\text{cal}}$ ” is the number of in-distribution calibration spectra in the predicted-class partition; “ $n_{\text{test}}$ ” the number of rare-set spectra routed to that class.

Pred. class	$n_{\text{cal}}$	$n_{\text{test}}$	Coverage	Detection
Ia	850	7	0.969	1.00
Ibc	253	34	0.971	1.00
II	414	45	0.960	1.00
SLSN	32	21	0.957	1.00
AGN	18	13	1.000	1.00
TDE	42	20	0.787	1.00
CV	60	149	0.917	0.919

behaviour of the per-class Mondrian quantile. Rare-set detection at this operating point is 100% for every predicted class except CV (91.9%), which absorbs the bulk of the Blazar, QSO, and Novae mis-predictions – the quantitative formulation of the per-class pattern of Sec. V E.

*d. AD-conditional coverage diagnostic.* The Mondrian guarantee is *marginal*: it ensures  $1 - \alpha$  coverage averaged over the in-distribution distribution but not conditional on the AD score itself. Stratifying the held-out set into AD-score quintiles reveals that coverage is 1.000 in Q1–Q4 (the 80% of spectra whose AD score lies far below the per-class thresholds, by construction always covered) and only 0.754 in Q5 (the top 20%, where survey-mode triage actually fires). The full 5% miscalibration budget is concentrated in Q5 – a known mathematical property of marginal conformal predictors stratified by their own score [29, 68, 69], not a calibration failure. Operationally, at the deployed  $\alpha = 0.05$  threshold the conditional false-alarm rate in the high-AD regime is closer to 25% than 5%. Sec. VI H introduces the AD-stratified estimator (AD-MCP) that fixes this directly.

### B. Adaptive prediction sets for classification

The conformal machinery applied to the classifier’s softmax output yields per-spectrum *prediction sets* of plausible labels. Following Romano *et al.* [69], we use the class-conditional nonconformity score

$$s_{\text{clf}}(x, y) = 1 - p_{\text{fine}}(y | x), \quad (3)$$

and define the adaptive prediction set (APS) at coverage  $1 - \alpha$  as  $\mathcal{C}_\alpha(x^*) = \{y : p_{\text{fine}}(y | x^*) \geq 1 - \hat{q}_\alpha\}$ , with  $\hat{q}_\alpha$  the finite-sample-corrected empirical  $(1 - \alpha)$ -quantile of  $s_{\text{clf}}$  on the calibration set.

At the  $\alpha = 0.10$  operating point, ID prediction sets are singletons for 89% of inputs while OOD prediction sets are singletons for 77.5% – the model committed to a wrong class, the disguised-class regime of Table X. At the stricter  $\alpha = 0.05$  level OOD sets broaden substantially (mean 1.82 vs ID mean 1.37), reflecting genuine uncertainty between physically related classes (e.g. a Ca-rich spectrum produces {Ibc, II}). A broadened set of size  $\geq 3$  is operationally more useful than an over-confident

point prediction. At the loose  $\alpha = 0.20$  point, 40% of OOD spectra produce an *empty* prediction set – the conformal procedure formally declining to classify, a strong “probably not any known class” signal distinct from the AD flag.

### C. Aleatoric/epistemic decomposition via deep ensembles

The conformal procedure provides distribution-free calibration but does not distinguish two qualitatively different sources of uncertainty. We supplement it with the standard predictive-entropy decomposition arising from the deep ensemble of  $M = 6$  ASTRANet variants. Writing  $\bar{p}(y | x) = M^{-1} \sum_m p^{(m)}(y | x)$ ,

$$H[\bar{p}] = \frac{1}{M} \sum_{m=1}^M H[p^{(m)}] + \text{MI}(y; \theta | x), \quad (4)$$

where the first term is *aleatoric* (data noise over which models agree) and the second *epistemic* (model-to-model disagreement). MI is high precisely when the input is out of distribution and the variants extrapolate inconsistently. In the framework MI is not a primary detector – the LightGBM ensemble outperforms it by a large margin (AUROC  $\sim 0.996$  vs  $\sim 0.78$ ) – but an *interpretation overlay*: high LightGBM score *and* high MI means the ensemble disagrees about identity (a genuinely novel object, Regime C); high LightGBM score *and* low MI means the ensemble agrees it is far from any class manifold (a disguised-class object, Regime B).

### D. The confidence-aware output

For each spectrum the framework returns a five-component output:

1. a fine-class point prediction  $\hat{y}$  (Sec. IV A);
2. a Mondrian conformal p-value  $p_M(x)$  (Eq. 2). Equivalently,  $p_{\text{wrong}}(x) \equiv 1 - p_M(x) \in [0, 1]$  is a per-sample, distribution-free, finite-sample-calibrated probability that the commitment to  $\hat{y}$  is mistaken, valid under arbitrary distribution shift provided the calibration set remains exchangeable;
3. an adaptive prediction set  $\mathcal{C}_\alpha(x)$  at coverage  $1 - \alpha$  (Eq. 3);
4. per-class ensemble probability intervals  $\{\bar{p}_k \pm \sigma_k\}_{k=1}^{K_f}$  from the  $M=6$  variants (Sec. VI E);
5. an aleatoric/epistemic decomposition of the predictive entropy (Eq. 4).

All five are produced from a single forward pass through the deep ensemble ( $< 200$  ms per spectrum on a single

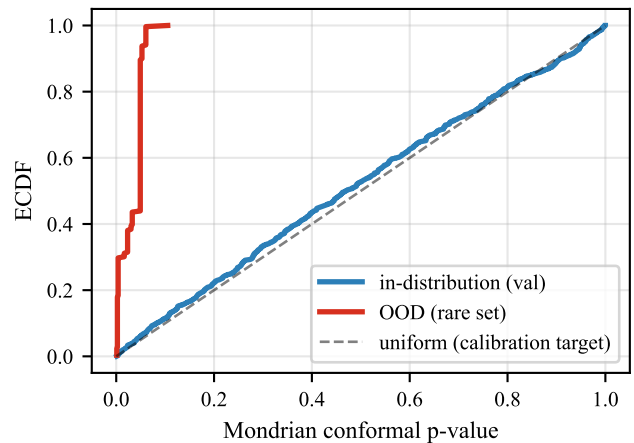


FIG. 4. Mondrian conformal p-value distribution on the in-distribution held-out validation set (blue) and the 289-spectrum rare set (red). The ID distribution is statistically indistinguishable from uniform (diagonal), confirming exchangeability between calibration and held-out validation. The OOD distribution piles near 0: 99.7% of rare spectra have  $p_M < 0.10$  and 89.6% have  $p_M < 0.05$ .

GPU) and together answer: *is this spectrum anomalous* (the p-value); *which classes are plausible* (the APS); *what is the per-class probability and its spread* (the intervals); *is the classifier overconfident* (the epistemic term); and *has the framework declined to commit* (an empty APS).

### E. Per-class ensemble probability intervals

For a survey operator deciding which physical interpretations to act on, none of the four components above directly answers “*what is the calibrated probability of class  $k$ , and how uncertain is that probability across the ensemble?*” Writing  $p^{(m)}(y | x)$  for the  $m$ -th variant’s predictive distribution, we define

$$\begin{aligned} \bar{p}_k(x) &= \frac{1}{M} \sum_{m=1}^M p^{(m)}(y=k | x), \\ \sigma_k(x) &= \sqrt{\frac{1}{M-1} \sum_{m=1}^M (p^{(m)}(y=k | x) - \bar{p}_k(x))^2} \end{aligned} \quad (5)$$

and report the  $K_f$  intervals  $\bar{p}_k(x) \pm \sigma_k(x)$  at zero additional cost from the per-model softmaxes the ensemble already produces.

*a. Operational behaviour across the five regimes.* The information content of  $\{\bar{p}_k, \sigma_k\}$  is sharply regime-dependent (Table VI). For Regime I (the disguised Blazar AT 2024uln), all six variants concur on CV at  $\bar{p}_{\text{CV}} = 92.7\% \pm 4.9\%$ . This is the empirical *absence* of an ensemble-internal anomaly signal: the classifier-internal UQ axis – the same one that powers softmax entropy, MC-dropout variance, and conformal-on-softmax  $p_{\text{wrong}}$

– has nothing to flag, because all six members arrive at the same confident wrong commitment. The detection signal must come from outside the classifier head: the cross-family AD-layer p-value  $p_M = 0.046$ , carried entirely by embedding-space distance and density scores. For Regimes II–V the top-class spread is large ( $> 10\%$ ), reflecting genuine ensemble disagreement that classifier-internal UQ alone would detect. The Regime I contrast – tight consensus ( $\sigma_{\hat{y}} \approx 5\%$ ) on a wrong class versus a flagged  $p_M = 0.046$  on the same spectrum – is the concrete demonstration that classifier-internal UQ and cross-family AD are *structurally complementary* axes, not interchangeable implementations of one estimator.

#### F. Test-error uncertainty: the two UQ axes catch different failure modes

We establish the structural complementarity of Sec. VIE at population scale on the held-out in-distribution test set:  $N_{\text{err}} = 456$  mis-classifications out of  $N_{\text{test}} = 3,396$  spectra. For each spectrum we compute six classifier-internal UQ signals (top-1 confidence, predictive entropy, top-1/top-2 margin, mutual information, predicted-class ensemble spread  $\sigma_{\hat{y}}$ , and model disagreement) and, in parallel, the cross-family AD score  $s_{\text{AD}}$ ; each is evaluated as an error detector (Table VII).

*a. Per-class anatomy: Regime-I disguise within the in-distribution set.* The per-class breakdown of  $\sigma_{\hat{y}}$  on errors (Fig. 5) reveals a Regime-I-like pattern inside the in-distribution test set. Rare/hard classes (SLSN 16.2%, CV 14.1%, TDE 13.3%) show large ensemble spread on errors – classifier-internal UQ has a clean signal to fire on. The dense CC classes (Ibc 9.1%, II 10.8%) show the smallest spread *even on errors* – the ensemble is confidently wrong, exactly the predicted-class destinations of the Regime-I OOD spectra of Sec. VE. Within this regime classifier-internal UQ is silent by construction; only the cross-family AD layer can detect the failure.

*b. Summary.* The Regime-I Blazar contrast and this population-level analysis jointly establish that the two UQ axes of ASTRANet-CP are structurally orthogonal detectors of different failure modes. Classifier-internal UQ dominates on in-distribution boundary errors (AUROC 0.895 vs 0.830); cross-family AD dominates on OOD Regime-I disguise. ASTRANet-CP deploys both, and reports both for every input.

#### G. Selective classification with AD-orthogonal abstention

The structural complementarity above has a direct operational consequence: the framework can *refuse to commit* when classifier-internal UQ is low, without compromising the AD layer. We call this *AD-orthogonal abstention* – the abstention decision is taken on the UQ axis (which catches in-distribution boundary errors), the

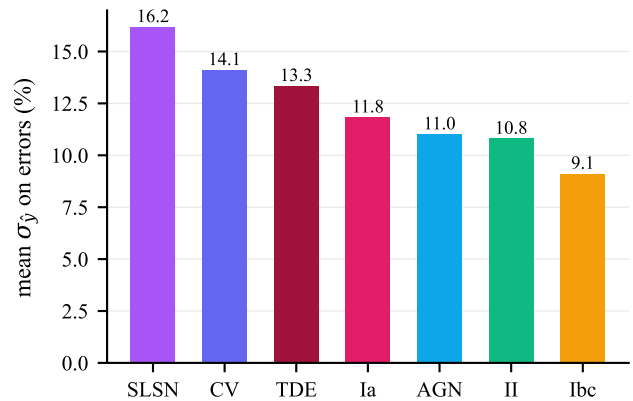


FIG. 5. Mean predicted-class ensemble spread  $\bar{\sigma}_{\hat{y}}$  on mis-classifications, by predicted class. Rare/hard classes (SLSN, CV, TDE) show large  $\sigma_{\hat{y}}$  on errors; the dense CC classes (Ibc, II) show the smallest  $\sigma_{\hat{y}}$  even on errors – the ensemble is confidently wrong, in direct analogy to the Regime-I OOD pattern. These dense classes absorb the bulk of rare-class confusions and are where the cross-family AD layer is necessary as a UQ axis independent of the classifier head.

anomaly decision independently on the AD axis (which catches Regime-I-style disguise).

*a. Selective accuracy.* Using top-1 confidence as the abstention signal (Table VIII), dropping the most uncertain 10% of predictions lifts selective accuracy from 0.866 to 0.912 (+4.7 pp).

*b. AD-orthogonality.* Across all coverage levels (Table VIII, last column), 67–81% of the spectra rejected by the abstention rule have an AD score *below* the operational 95th-percentile threshold of ASTRANet-Sentinel – in-distribution boundary cases, the dense Ibc/II/CV regime of Sec. VIF. The two operational rules target substantially disjoint populations.

*c. Three-way operational policy.* The framework therefore supports a three-way decision on two independent axes:

- **COMMIT:**  $\hat{p}_{\text{top1}} \geq \tau_{\text{abstain}}$  and  $s_{\text{AD}} < \tau_{\text{AD}}$  – return the point prediction with calibrated confidence.
- **ABSTAIN:**  $\hat{p}_{\text{top1}} < \tau_{\text{abstain}}$  and  $s_{\text{AD}} < \tau_{\text{AD}}$  – refuse to commit; forward for human review.
- **ALERT:**  $s_{\text{AD}} \geq \tau_{\text{AD}}$  – flag as anomalous regardless of the UQ axis.

With  $\tau_{\text{abstain}}$  at the 10th-percentile calibration confidence and  $\tau_{\text{AD}}$  at the 95th-percentile  $s_{\text{AD}}$ , the framework delivers  $\sim 91\%$  selective accuracy on committed predictions while preserving the 100%-recall rare-anomaly capability of Sec. VD. To our knowledge this is the first deployment of AD-orthogonal selective classification in transient spectroscopy.

TABLE VI. Per-class ensemble probability intervals  $\{\bar{p}_k \pm \sigma_k\}$  (Eq. 5) on representative case-study spectra from each of the five physical regimes of Sec. II, paired with the cross-family AD-layer Mondrian p-value  $p_M$ . Only the top three classes by  $\bar{p}_k$  are shown. Regime I exhibits tight consensus ( $\sigma_{\hat{y}} \lesssim 3\%$ ) on a wrong class with  $p_M$  carrying the entire detection signal; Regimes II–V exhibit large  $\sigma$  ( $> 10\%$ ) reflecting genuine ensemble disagreement.

Regime	Object	True class	Class 1	Class 2	Class 3	$p_M$
I	AT 2024u1n	Blazar	CV 92.7% $\pm$ 4.9%	Ibc 2.5% $\pm$ 2.0%	II 1.8% $\pm$ 1.8%	0.046
II	2021zfp	Ca-rich	CV 46.1% $\pm$ 14.4%	Ibc 30.5% $\pm$ 15.1%	II 19.3% $\pm$ 5.3%	$\sim 0.12$
III	AT2021lfa	afterglow	CV 76.1% $\pm$ 21.7%	SLSN 17.9% $\pm$ 20.0%	TDE 2.4% $\pm$ 1.5%	$\ll 0.01$
IV	AT 2024wpp	FBOT	CV 71.6% $\pm$ 19.7%	II 11.4% $\pm$ 10.1%	Ibc 7.8% $\pm$ 6.9%	$\sim 0.009$
V	AT2022cva	long GRB	TDE 51.8% $\pm$ 18.2%	SLSN 26.6% $\pm$ 17.7%	CV 14.9% $\pm$ 3.1%	$\sim 0.087$

TABLE VII. Error-detection AUROC of each UQ signal on the held-out ID test set ( $N_{\text{test}} = 3,396$ ,  $N_{\text{err}} = 456$ ). Classifier-internal signals lead the cross-family AD score by 0.065 in AUROC at the top of the table.

UQ signal	AUROC
Top-1 confidence $\hat{p}_{\text{top1}}$	<b>0.895</b>
Top-1/top-2 margin $\Delta$	0.890
Predictive entropy $H$	0.876
Mutual information MI	0.806
Ensemble spread $\sigma_{\hat{y}}$	0.792
Model disagreement	0.754
Cross-family AD score $s_{\text{AD}}$	0.830
<b>Gap (best internal – AD)</b>	<b>0.065</b>

TABLE VIII. Selective classification using top-1 confidence as the abstention signal on the full held-out test set ( $N = 3,396$ ). Each row drops the top- $X\%$  most uncertain test spectra. “AD-low %” is the fraction of *rejected* spectra whose AD score lies below the 95th-percentile threshold of **ASTRANet-Sentinel**.

Coverage	Selective acc.	Gain (pp)	AD-low %
1.00 (baseline)	0.866	—	—
0.95 (drop 5%)	0.890	+2.4	66.9%
<b>0.90 (drop 10%)</b>	<b>0.912</b>	<b>+4.7</b>	<b>72.0%</b>
0.80 (drop 20%)	0.946	+8.1	80.7%
0.70 (drop 30%)	0.972	+9.9	84.9%

## H. AD-stratified Mondrian Conformal Prediction

The AD-conditional diagnostic of Sec. VIA showed that marginal Mondrian concentrates its 5% miscalibration budget in the high-AD operational regime (0.824  $\pm$  0.030 coverage in Q5 vs nominal 0.95). This is the expected profile of marginal conformal predictors stratified by their own score [68, 69] and is operationally suboptimal.

*a. Method.* We introduce *AD-stratified Mondrian Conformal Prediction* (AD-MCP). Let  $q(s_{\text{AD}}(x)) \in \{1, \dots, Q\}$  denote the AD-score quintile under bin edges fitted on the calibration set. For each (predicted class  $c$ , AD-quintile  $q$ ) cell we compute

$$\tau_{c,q} = \text{Quantile}_{1-\alpha}(\{s(x_i) : \hat{y}_i = c, q(s_{\text{AD}}(x_i)) = q\}), \quad (6)$$

with  $s(x) = 1 - \hat{p}(\hat{y}(x) | x)$ . A test point fires if  $s(x) > \tau_{c,q}$ . Cells with fewer than  $n_{\text{min}} = 10$  calibration samples fall back to the marginal class threshold  $\tau_c$ ; with 1,669 calibration samples and  $Q = 5$  this activates only for sparse (rare-class, extreme-quintile) cells, not for the dominant Ia/II/CV classes. Under within-cell exchangeability AD-MCP satisfies the conditional coverage guarantee

$$\Pr(s(x^*) \leq \tau_{c,q} | \hat{y}(x^*) = c, q(s_{\text{AD}}(x^*)) = q) \geq 1 - \alpha, \quad (7)$$

strictly stronger than the marginal guarantee of vanilla Mondrian. Building on atypicality-stratified conformal calibration [29], who stratify APS/RAPS by confidence and single-score atypicality for in-distribution coverage, AD-MCP stratifies instead by a learned cross-family anomaly ensemble crossed with predicted class. To our knowledge it is the first such estimator deployed for out-of-taxonomy discovery in spectroscopic transient triage.

*b. Empirical validation.* Under 5-fold cross-validation on the in-distribution held-out set (Table IX), AD-MCP achieves uniform  $0.952 \pm 0.001$  coverage across all five quintiles, including the operationally critical Q5 (0.953). Marginal Mondrian over-covers in Q1–Q3 and under-covers in Q5 (0.824), a standard deviation across quintiles of 0.066 – a factor  $\sim 80$  larger than AD-MCP’s 0.0008. Both achieve the same marginal coverage averaged across quintiles (0.952), but only AD-MCP delivers it *uniformly*.

*c. Width-coverage trade-off and BOOM integration.* Uniform conditional coverage is bought with smaller per-cell sample sizes ( $n_{c,q} \approx 47$  vs  $n_c \approx 233$  marginal); the net effect is the conditional-vs-marginal trade-off predicted by Vovk *et al.* [67] theory – AD-MCP exchanges marginal sharpness in Q1–Q3 for conditional validity in Q5, the operationally relevant property. Under the planned BOOM integration the rolling calibration window will accumulate  $\sim 10^4$  ID spectra, exceeding  $n_{\text{min}}$  for all cells and removing the fallback dependence. AD-MCP is the conformal layer intended for offline production triage at  $\alpha = 0.05$ .

TABLE IX. Per-quintile empirical Mondrian conformal coverage at  $\alpha = 0.05$  on the in-distribution held-out set, under 5-fold cross-validation. AD-MCP (this work) achieves uniform 0.95 coverage across AD-score strata; marginal Mondrian over-covers in Q1–Q3 and under-covers in Q5 by 0.13.

Quintile	Marginal Mondrian	AD-stratified Mondrian (this work)	Improvement
Q1 (low AD)	1.000	0.9512	−0.049 (toward nominal)
Q2	1.000	0.9519	−0.048 (toward nominal)
Q3	0.989	0.9514	−0.038 (toward nominal)
Q4	0.947	0.9521	+0.006
<b>Q5 (high AD, operational)</b>	<b>0.824</b>	<b>0.9534</b>	<b>+0.129</b> (toward nominal)
Std across $\{Q1, \dots, Q5\}$	0.066	<b>0.0008</b>	$\sim 80\times$ tighter

## VII. CASE STUDIES: THE FIVE FAILURE MODES RESOLVED

We now revisit the five failure-mode regimes of Sec. II from the operational perspective of the deployed framework. For each regime we give the five-component confidence-aware output and an astrophysical interpretation; the per-spectrum anomaly scores for all seven case-study spectra are in Table X, and the per-class ensemble intervals in Table VI. Our goal is not to repeat numbers already given but to show how the framework’s outputs jointly distinguish the five regimes for a survey operator.

### A. Regime I – Continuum-disguised AGN-class: AT 2024u1n

The Blazar AT 2024u1n is the canonical case of continuum-disguised AGN-class events. The classifier maps the spectrum confidently to CV ( $\hat{p}_{CV} = 0.927$ ), the predicted-class entropy is low, and the within-class typicality is below unity – the embedding is mapped *inside* the typical radius of its predicted CV class. Only a single family-only mini-ensemble fires weakly at 1% FAR, yet the cross-family LightGBM ensemble assigns  $s_{\text{ens}} = 0.927$ . The confidence-aware output at  $\alpha = 0.05$  is

$$(\hat{y}, p_M, \mathcal{C}_{0.05}, H_{\text{epi}}) = (\text{CV}, 0.046, \{\text{CV}\}, \text{low}). \quad (8)$$

The Mondrian p-value flags the spectrum; the prediction set is a singleton on the wrong class; the low epistemic uncertainty (all six ensemble variants agree on CV) confirms the failure mode is *disguise*, not *model disagreement*. A high anomaly score on a confident-singleton prediction is the textbook signature of Regime I.

*a. Classifier-internal UQ alone misses Regime I.* The per-sample  $p_{\text{wrong}}$  output of component (ii) of Sec. VID, computed against the CV-predicted calibration distribution, yields  $p_{\text{wrong}}(x) = 0.67$  for this spectrum – a moderate signal, well above the  $\alpha = 0.05$  threshold:  $\hat{p}_{CV} = 0.927$  places the Blazar in the lower-confidence half of CV-predicted calibration samples (typical confidence  $\geq 0.95$ ) but not in the extreme tail. Classifier-internal uncertainty alone – whether softmax confidence or conformal-on-softmax as here – is structurally incapable of catching this regime: the failure

mode *is* a confident wrong commitment, by definition. The strong signal ( $p_M = 0.046$ , a factor  $\sim 15\times$  stronger than  $p_{\text{wrong}}$ ) is carried entirely by the cross-family AD layer. This single contrast –  $p_{\text{wrong}} = 0.67$  versus  $p_M = 0.046$  on the same spectrum – is the empirical case for the cross-family AD layer over any classifier-internal UQ, and is the principal methodological argument of the paper.

Physically, this is consistent with the Blazar’s continuum-dominated optical spectrum at the epoch of observation, the underlying AGN power-law continuum overlapping the accretion continuum of cataclysmic variables in the wavelength range accessible to SEDM.

### B. Regime II – Spectroscopic disguise: 2021zfp and novae

The Ca-rich transient 2021zfp is the archetype of spectroscopic disguise within physical neighbours. The classifier predicts CV with low confidence ( $\hat{p}_{CV} = 0.46$ ); fine-head entropy is elevated; within-class Mahalanobis is moderately high; HEC is the highest of any case-study spectrum. Only one cascade method fires at 1% FAR, but the cross-family ensemble integrates the moderate signals into  $s_{\text{ens}} = 0.907$ . The confidence-aware output is

$$(\hat{y}, p_M, \mathcal{C}_{0.10}) = (\text{CV}, \sim 0.12, \{\text{CV}, \text{Ibc}, \text{II}\}), \quad (9)$$

where the APS prediction set at  $\alpha = 0.10$  contains, alongside the point prediction, the two physically plausible classes (stripped-envelope or H-rich CC). This is the genuinely informative case: the wide prediction set with near-equal ensemble mass on Ibc ( $30.5\% \pm 15.1\%$ ) tells the operator the framework refuses a confident CV commitment. The novae populations show the same behaviour at scale: of 67 Novae in the rare set, 4 are caught by any family alone but 54/67 by the full cross-family pipeline – the strongest population-scale demonstration of cross-family complementarity in the paper.

### C. Regime III – Continuum-dominated: AT20211fa

The GRB afterglow AT20211fa [70] represents continuum-dominated mis-classifications where, unlike

TABLE X. Per-class case study illustrating complementarity in both directions, with scores read directly from the production run. *Regime A* (top): high-confidence cases where uncertainty-based scores do not fire; detection is driven by within-class Mahalanobis and GMM, and the distance and density family ensembles both fire. *Regime B* (middle): high-confidence cases where the embedding itself is deceived (typicality  $< 1$ ) and no single-family mini-ensemble fires at 1% FAR; detection comes from cross-family non-linear combination only. *Regime C* (bottom): low-confidence near-OOD cases where uncertainty fires but is borderline; distance/density evidence carries the sample over threshold. “Conf.” is fine-head confidence; “Entropy” fine-head softmax entropy; “Typ.” within-class typicality; “Mahal.” within-class Mahalanobis distance; “iForest” the isolation-forest score; “HEC” the hierarchical entropy combination; “Fam.” the number of family-only mini-ensembles (of four) that flag the spectrum at 1% FAR;  $s_{\text{ens}}$  the LightGBM ensemble score. Bold marks the dominant detection score(s) per row; bold **0** in “Fam.” highlights the Regime-B spectra no family alone catches.

Object ID	True class	Pred.	Conf.	Entropy	Typ.	Mahal.	iForest	HEC	Fam.	$s_{\text{ens}}$
<i>Regime A – uncertainty fails (high confidence, low entropy)</i>										
AT2021lfa	afterglow	CV	0.761	0.77	1.24	<b>61.0</b>	<b>0.54</b>	0.97	2	0.991
AT 2026dbl	FBOT	CV	0.757	0.85	1.21	<b>55.0</b>	<b>0.51</b>	1.03	2	0.990
<i>Regime B – both UQ and distance fail (typicality <math>\lesssim 1</math>, at most one family-only mini-ensemble fires)</i>										
AT 2024uln	Blazar	CV	0.927	0.38	0.87	24.0	0.52	0.44	1	0.927
AT 2024wpp	FBOT	CV	0.716	0.98	1.15	44.0	0.48	1.40	<b>0</b>	0.977
<i>Regime C – corroboration: uncertainty fires but borderline</i>										
AT2022cva	long GRB	TDE	0.518	<b>1.24</b>	1.30	22.0	0.53	<b>1.66</b>	2	0.824
2021vdr	ILRT	II	0.337	<b>1.25</b>	0.97	12.0	0.48	<b>1.98</b>	0	0.815
2021zfp	Ca-rich	CV	0.461	1.22	1.26	40.0	0.51	<b>2.09</b>	1	0.907

Regime I, the embedding is genuinely far from the predicted-class centroid: within-class Mahalanobis is in the extreme tail and the isolation forest fires, so both the distance and density family ensembles fire independently. The output  $(\hat{y}, p_M, \mathcal{C}_{0.05}, H_{\text{epi}}) = (\text{CV}, \ll 0.01, \{\text{CV}\}, \text{high})$  places the spectrum in the extreme anomaly tail of the CV calibration distribution despite the classifier’s commitment. 16 of the 17 afterglow spectra in the rare set are recovered at the  $\alpha = 0.10$  operating point.

#### D. Regime IV – Ambiguous progenitor: the FBOT class

FBOTs are the largest near-OOD class in our rare set ( $N = 98$ ) and the textbook ambiguous-progenitor regime. Predictions scatter across CV, TDE, Ia, and Ib; family-vote counts span the full 0–4 range. The framework’s behaviour is correspondingly heterogeneous: the APS sets widen substantially as  $\alpha$  tightens from 0.05 to 0.01 (mean ID set size grows from 1.4 to 2.1; the framework refuses to commit). The most interesting FBOT is AT 2024wpp, structurally close to Regime I (confident CV prediction, no family flagging) but physically distinct – the FBOT spectrum genuinely overlaps with CV templates at certain phases due to the blue continuum. The framework flags both as anomalous; the physical distinction between Regimes I and IV must be made downstream with light-curve and host-galaxy information [12, 30, 31].

#### E. Regime V – Far-OOD: AT2022cva

The long GRB AT2022cva is the textbook far-OOD case. The classifier assigns it to TDE with moderate confidence (0.52); fine-head entropy is among the highest of the case-study spectra; two families produce moderate signal. The output  $(\hat{y}, p_M, \mathcal{C}_{0.10}, H_{\text{epi}}) = (\text{TDE}, \sim 0.087, \{\text{TDE}, \text{SLSN}\}, \text{high})$  exhibits high epistemic uncertainty ( $\sigma_{\text{TDE}} = 18.2\%$ ) – the ensemble variants disagree about the classification. This is the diagnostic for Regime V: the failure is genuine novelty, not disguise.

*a. Summary.* The five case studies confirm the design implication of Sec. II: the five-component output jointly distinguishes disguise (Regime I/II – singleton prediction set on a wrong class, low MI, and for Regime I tight ensemble consensus on the wrong class), continuum-dominated mis-classification (Regime III – far-from-centroid embedding), genuine ambiguity (Regime IV – broad prediction set with epoch-dependent intervals), and novelty (Regime V – broad prediction set with high MI). No single component suffices, and the Regime I contrast between tight ensemble consensus ( $\sigma_{\text{CV}} \approx 5\%$ ) and a flagged Mondrian p-value ( $p_M = 0.046$ ) is the empirical case for cross-family AD as a structurally distinct UQ axis.

## VIII. DISCUSSION AND CONCLUSIONS

We have presented ASTRANet, a confidence-aware framework for spectroscopic transient discovery built from a hierarchical classifier that operates on observer-frame spectra without host redshift or spectral phase, a cross-family anomaly detection layer

(ASTRANet-Sentinel), and a conformal uncertainty layer (ASTRANet-CP). Two arguments organise the work. The first is physical: the failure modes of closed-set spectroscopic classifiers are not a uniform softmax-overconfidence phenomenon but separate into five regimes with distinct anomaly-score signatures, two of which – continuum-disguised AGN-class events and spectroscopic disguise within physical neighbours, together  $\sim 43\%$  of our rare population – are recoverable only through cross-family non-linear combination. The second is statistical: classifier-internal uncertainty and embedding-based anomaly detection are structurally complementary axes, dominating on in-distribution boundary errors and out-of-distribution disguise respectively, and should be deployed together rather than interchangeably.

*a. What the framework enables.* Operationally, the framework converts spectroscopic triage from an uncalibrated judgment into allocation under quantified risk: each candidate carries a conformal p-value, a prediction set of plausible classes, and an aleatoric/epistemic decomposition, so that high-AD high-MI candidates (novel and ambiguous) can be separated from high-AD low-MI candidates (novel but confidently mislabelled – the disguised-class regime) and from routine low-AD candidates. The finding that  $\sim 43\%$  of the rare population is caught by no single anomaly-score family means a pipeline built on softmax confidence, Mahalanobis distance, or isolation forest alone silently loses roughly half this population by construction; the framework is the smallest machinery that recovers it. We are preparing the framework for offline production integration with the ZTF BOOM broker [27] as a daily batch pipeline delivering anomaly reports to a Slack alert channel; the spectroscopic follow-up campaign of flagged anomalies will be reported in companion work.

*b. Why embedding-based scores work.* Modern networks produce overconfident softmax outputs on OOD inputs [19, 20], which translates directly into weak logit-space OOD detection. The embedding space, structured by the supervised-contrastive loss, instead encodes distance from the training manifold: an OOD spectrum need not look uncertain in logit space, only far from in-distribution embeddings, which the Mahalanobis and GMM scores quantify directly. Averaging embeddings across the  $M = 6$  ensemble variants further stabilises these distances.

*c. Limitations.* Several limitations bound the present results. *Sample size:* the Ca-rich ( $N = 10$ ) and Classical Nova ( $N = 8$ ) classes are the smallest in the rare set and also the strongest Regime II disguise cases, so their per-class recovery is the most uncertain. *Single modality:* the framework uses one spectroscopic epoch, yet the hardest near-OOD cases (Ca-rich vs Ibc, ILRT vs Iib, FBOT vs TDE) are separable photometrically within a few epochs – a multi-modal extension ingesting light curves and host imagery, in the spirit of AppleCiDer [28], is the natural next step and is enabled

by the embedding-based architecture.

Relative to prior transient anomaly detection, which has focused on photometric light curves [21, 22, 24], the closest methodological prior is the distance-metric-ensemble paradigm of DiMMAD [23], itself built on the DistClassiPy distance-based classifier [71]. DiMMAD ensembles 16 distance metrics — i.e. distinct geometries over a single photometric feature space — and reports that multi-metric consensus excels precisely at off-manifold OOD discovery while a single isolation forest remains competitive for rare in-distribution subtypes. ASTRANet generalises this paradigm along an orthogonal axis: rather than ensembling geometries of one distance notion, it combines four physically motivated score families (distance, density, energy/uncertainty, and hierarchical hybrids) non-linearly over learned spectroscopic embeddings, with calibrated prediction sets. This distinction is what lets the cross-family combiner recover the near-OOD, disguised-class regime (Regimes I–II) where any single family — distance included — falls below threshold.

*d. The path to LSST.* The Vera C. Rubin Observatory will discover  $\sim 10^6$  transient candidates per year, of which  $\sim 10^4$  will receive spectroscopic follow-up via e.g., 4MOST-TiDES [72, 73] and SOXS [74]. Beyond these near-term facilities, proposed next-generation spectroscopic arrays — e.g. an array of  $>100$  AO-enabled 1–4 m telescopes for time-critical transient spectroscopy [75] — would push follow-up capacity further still; in every such regime, automated confidence-aware triage is the prerequisite for deciding which spectra such an array should target. At this rate triage cannot remain a human-in-the-loop process, and every 1% improvement in confidence-aware triage corresponds to  $\sim 10^2$  peculiar transients per year that would otherwise be lost to routine classification. The framework is scalable to this regime by design: inference is below survey cadence, the conformal calibration is distribution-free and recalibrable nightly, and the failure-mode taxonomy extends to any near-degenerate class the training distribution under-samples. To our knowledge this is the first systematic application of confidence-aware multi-category anomaly detection and uncertainty quantification to astronomical spectroscopy; frameworks of this kind will be required – not optional – for discovery in the Rubin era.

## ACKNOWLEDGMENTS

The UMN authors acknowledge support from the National Science Foundation with grant numbers PHY-2117997, PHY-2308862 and PHY-2409481. A.S. and M.C. acknowledge support from LSST-DA through grants 2025-SFF-LFI-14-Coughlin and 2026-SFF-LFI-17-Sasli. LINCC Frameworks is supported by Schmidt Sciences, a philanthropic initiative founded by Eric and Wendy Schmidt, as part of the Virtual Institute of As-

trophysics (VIA).

Based on observations obtained with the Samuel Oschin Telescope 48-inch and the 60-inch Telescope at the Palomar Observatory as part of the Zwicky Transient Facility project. ZTF is supported by the National Science Foundation under Grants No. AST-1440341, AST-2034437, and currently Award #2407588. ZTF receives additional funding from the ZTF partnership. Current members include Caltech, USA; Caltech/IPAC, USA; University of Maryland, USA; University of California, Berkeley, USA; Cornell University, USA; Drexel University, USA; University of North Carolina at Chapel Hill, USA; Institute of Science and Technology, Austria; National Central University, Taiwan, German Center for Astrophysics, Germany, and OKC, University of Stockholm, Sweden. Operations are conducted by Caltech’s Optical Observatory (COO), Caltech/IPAC, and the University of Washington at Seattle, USA.

SED Machine is based upon work supported by the National Science Foundation under Grant No. 1106171. The Gordon and Betty Moore Foundation, through both the Data-Driven Investigator Program and a dedicated grant, provided critical funding for SkyPortal.

## Appendix A: Detailed architecture

This appendix expands the high-level description of ASTRANet given in Sec. IV A. The model takes a two-channel 1D signal  $(B, 2, L)$  of length  $L = 4096$  as input: the robust-scaled flux and its Savitzky–Golay first derivative [window 7, polynomial order 3; 76], computed *after* augmentation.

*a. Multi-scale stem.* Three parallel convolutional branches with kernel sizes  $k \in \{7, 31, 151\}$  each apply a 1D convolution, group normalisation [8 groups; 77], GELU activation [78], and dropout, each producing  $C = 32$  channels. Outputs are concatenated and fused through a  $1 \times 1$  convolution to a  $C_{\text{base}} = 96$ -channel map. Temporal average pooling with stride 4 reduces sequence length, and a final  $1 \times 1$  projection expands to the embedding size  $d_{\text{emb}} = 192$ .

*b. Dilated TCN backbone.* Six residual blocks [52], each with two convolutional layers (kernel size 5, group normalisation, GELU): the first layer uses exponentially increasing dilation  $r_i = 2^{i \bmod 6}$ , the second uses dilation 1. A residual skip connection adds the block input to its output. Stochastic depth [79] with linearly increasing drop probability  $0 \rightarrow 0.1$  provides implicit ensemble regularisation. Cumulative receptive field:  $\sim 250$  samples.

*c. Metadata conditioning via FiLM.* The metadata vector  $\mathbf{c} \in \mathbb{R}^{64}$  encodes three quantities: spectral phase  $\phi$  (rest-frame days from maximum light, represented as  $[\sin \phi', \cos \phi', \tanh \phi', \text{validity}]$  with  $\phi' = \phi/30$  d), host redshift  $z$  (as  $[\tanh(5z), \text{validity}]$ ), and an instrument-identifier embedding ( $N_{\text{inst}} = 16$ ,  $d_{\text{inst}} = 16$ ). A two-layer MLP ( $28 \rightarrow 128 \rightarrow 64$ ) with LayerNorm, GELU, and residual projection produces  $\mathbf{c}$ . The conditioning vector

modulates the feature map at two points via FiLM [25]:

$$\text{FiLM}(\mathbf{x}, \mathbf{c}) = \mathbf{x} \odot [1 + \gamma(\mathbf{c})] + \beta(\mathbf{c}), \quad (\text{A1})$$

with  $\gamma$  and  $\beta$  learned linear projections.  $\text{FiLM}_1$  acts after the stem, before the TCN;  $\text{FiLM}_2$  acts on the pooled embedding before the heads.

*d. Multi-head attention pooling.* Four heads ( $d_{\text{emb}}/H = 48$  dimensions each) score the TCN output via a small MLP ( $48 \rightarrow 24 \rightarrow 1$ ) and softmax over the sequence dimension. Head outputs  $\mathbf{v}_h = \sum_t \alpha_h(t) \mathbf{x}_h(t)$  are concatenated and linearly projected to the embedding  $\mathbf{e} \in \mathbb{R}^{192}$  (LayerNorm + dropout  $p = 0.15$ ). The attention entropy  $H_{\text{attn}} = H^{-1} \sum_h (-\sum_t \alpha_h(t) \log \alpha_h(t))$  enters the loss as a regularisation bonus.

*e. Hierarchical heads.* The coarse head ( $K_c = 3$  superclasses) is a two-layer MLP ( $192 \rightarrow 256 \rightarrow 3$ ) with LayerNorm, GELU, dropout  $p = 0.4$ . The fine head ( $K_f = 7$  classes) receives the embedding concatenated with the coarse softmax probabilities under stop-gradient (gradients flow only through the fine head), passed through a two-layer MLP ( $195 \rightarrow 384 \rightarrow 7$ ) with LayerNorm, GELU, dropout  $p = 0.5$ . Contrastive projection heads (3-layer MLPs  $192 \rightarrow 256 \rightarrow 256 \rightarrow 128$  for fine,  $192 \rightarrow 128 \rightarrow 128 \rightarrow 128$  for coarse) supply  $\ell_2$ -normalised vectors  $\mathbf{z}^{(\text{fine})}, \mathbf{z}^{(\text{coarse})}$  for the SupCon loss.

## Appendix B: Loss function and training procedure

*a. Loss function.* The total objective is:

$$\begin{aligned} \mathcal{L} = & w_f \mathcal{L}_{\text{focal}} + w_c \mathcal{L}_{\text{coarse}} \\ & + w_{\text{sc},f} \mathcal{L}_{\text{SupCon}}^{(\text{fine})} + w_{\text{sc},c} \mathcal{L}_{\text{SupCon}}^{(\text{coarse})} \\ & + w_{\text{conf}} \mathcal{L}_{\text{confusion}} - w_H H_{\text{attn}}, \end{aligned} \quad (\text{B1})$$

with weights listed in Table XI. The fine head uses focal loss [55] with label smoothing  $\epsilon = 0.05$  and class-specific  $\gamma_k$  ( $\gamma = 2$  default;  $\gamma_{\text{AGN}} = \gamma_{\text{TDE}} = 3$ ). The coarse head uses cross-entropy with the same smoothing. The supervised contrastive loss [54] is applied at temperature  $\tau = 0.07$  on both granularities (disabled on MixUp batches). The confusion penalty suppresses targeted misclassification pathways:  $(a \rightarrow b, w)$  pairs  $\{(TDE \rightarrow \text{Ia}, 0.5), (\text{SLSN} \rightarrow \text{Ibc}, 0.3), (\text{II} \rightarrow \text{Ibc}, 0.8)\}$  via a quadratic penalty on  $p(b | x)$  averaged over samples with true class  $a$ . The attention entropy bonus is subtracted (maximised) to keep attention spread.

TABLE XI. Loss term weights used in all experiments.

Term	Symbol	Weight
Focal (fine)	$w_f$	1.5
Cross-entropy (coarse)	$w_c$	0.3
SupCon (fine)	$w_{\text{sc},f}$	0.03
SupCon (coarse)	$w_{\text{sc},c}$	0.05
Confusion penalty	$w_{\text{conf}}$	0.5
Attention entropy	$w_H$	0.01

*b. Training procedure.* Five stochastic augmentations are applied per spectrum *before* the SG derivative is computed: sub-pixel wavelength shift ( $p = 0.3$ ,  $\delta \sim \mathcal{U}(-3, 3)$  pixels); multiplicative continuum warping ( $p = 0.3$ , 5-knot spline, amplitude  $\pm 0.05$ ); flux scaling ( $p = 0.4$ ,  $s \sim \mathcal{U}(0.85, 1.15)$ ); Gaussian noise ( $p = 0.5$ ,  $\text{SNR} \sim \mathcal{U}(10, 50)$ ); random masking of 1–3 contiguous regions covering 5–30% of the spectrum ( $p = 0.5$ ). At batch level, MixUp [57] is applied with  $p = 0.5$  and  $\lambda = \max(\lambda', 1 - \lambda')$ ,  $\lambda' \sim \text{Beta}(0.3, 0.3)$ . Class imbalance is addressed through effective-number-based over-sampling [58] with  $\beta = 0.9999$ . The optimiser is AdamW [56] with learning rate  $\eta_0 = 3 \times 10^{-4}$ , weight decay  $10^{-4}$ , gradient clip 1.0. The schedule uses a 5-epoch linear warmup followed by cosine annealing with warm restarts [80],  $T_0 = 30$ ,  $T_{\text{mult}} = 2$ ,  $\eta_{\text{min}} = 0.05 \eta_0$ . EMA [81] of model weights is maintained with decay  $\alpha = 0.996$  and used for all validation/test evaluations. Early stopping uses validation macro recall with patience 45 epochs (max 200 epochs). Full hyperparameter listing in Table XII.

TABLE XII. Hyperparameters for ASTRANet.

Parameter	Value
<i>Architecture</i>	
Input channels	2 (flux + SG deriv.)
SG filter (window / poly.)	7 / 3
Stem kernels	7, 31, 151
Base channels $C_{\text{base}}$	96
Embedding dim. $d_{\text{emb}}$	192
TCN depth $D$	6 blocks
TCN kernel size	5
Temporal downsample	4 $\times$
Attention heads $H$	4
Stochastic depth	0.0–0.1 (linear)
Dropout (backbone / emb.)	0.2 / 0.15
Normalisation	GroupNorm (8 groups)
Activation	GELU
Metadata output dim.	64
Instrument embeddings	16 $\times$ 16
Projection dim.	128
<i>Training</i>	
Batch size	128
Max epochs	200
Optimiser	AdamW
Learning rate $\eta_0$	$3 \times 10^{-4}$
Weight decay	$10^{-4}$
Gradient clip norm	1.0
LR warmup	5 epochs (linear)
LR schedule	Cosine warm restarts
$T_0 / T_{\text{mult}} / \eta_{\text{min}}$	30 / 2 / $0.05\eta_0$
EMA decay $\alpha$	0.996
MixUp $\alpha_{\text{mix}} / \text{prob.}$	0.3 / 0.5
Balanced sampling $\beta$	0.9999
Label smoothing $\epsilon$	0.05
Focal $\gamma$ (default)	2.0
$\gamma$ overrides	AGN=3, TDE=3, SLSN=2
SupCon temperature $\tau$	0.07
Early stopping patience	45 epochs

### Appendix C: The sixteen anomaly scores

Formal definitions of the 16 anomaly scores summarised in Sec. IV C. We adopt the convention *higher = more anomalous*. Let  $\mathbf{p} = \text{softmax}(\mathbf{z})$  be the fine-head softmax of an input with fine logits  $\mathbf{z} \in \mathbb{R}^{K_f}$ ,  $\mathbf{p}_c = \text{softmax}(\mathbf{z}_c)$  the coarse softmax,  $\mathbf{e}$  the embedding, and  $\{\boldsymbol{\mu}_k, \boldsymbol{\Sigma}_k\}_{k=1}^{K_f}$  the per-class mean and covariance of training embeddings.

*a. Uncertainty family (4 scores).*  $s_{\text{MSP}} = -\max_k p_k$ ;  $s_{\text{ent}} = -\sum_k p_k \log p_k$ ;  $s_{\text{en}} = -\log \sum_k \exp(z_k)$  (energy, 61);  $s_{\text{ODIN}} = -\max_k \text{softmax}(\mathbf{z}/T)_k$  with  $T = 1.5$  (temperature-only ODIN, 60).

*b. Distance family (6 scores; operate on  $\mathbf{e}$ ).* Global Mahalanobis  $s_{\text{Mglob}} = \sqrt{(\mathbf{e} - \boldsymbol{\mu})^\top \boldsymbol{\Sigma}^{-1} (\mathbf{e} - \boldsymbol{\mu})}$ ; class-min Mahalanobis  $s_{\text{Mclass}} = \min_k \sqrt{(\mathbf{e} - \boldsymbol{\mu}_k)^\top \boldsymbol{\Sigma}_k^{-1} (\mathbf{e} - \boldsymbol{\mu}_k)}$ ; within-prediction Mahalanobis (same formula, conditioned on  $\hat{y}_f$ );  $k$ -NN distance  $s_{k\text{NN}} = k^{-1} \sum_{j=1}^k \|\mathbf{e} - \mathbf{e}_{(j)}\|_2$  with  $k = 10$ ; cosine distance  $s_{\text{cos}} = 1 - \max_c \frac{\mathbf{z}^{(\text{fine})} \cdot \boldsymbol{\mu}_c^{(\text{fine})}}{\|\mathbf{z}^{(\text{fine})}\| \|\boldsymbol{\mu}_c^{(\text{fine})}\|}$  (in the contrastive projection space); typicality  $s_{\text{typ}} = \|\mathbf{e} - \boldsymbol{\mu}_{\hat{y}_f}\|_2 / R_{\hat{y}_f}$ , with  $R_k$  the 95th percentile of  $\|\mathbf{e}_i - \boldsymbol{\mu}_k\|_2$  over training samples of class  $k$ .

*c. Density family (4 scores).* Per-class GMM negative log-likelihood under the maximum-likelihood class; isolation forest [63] (200 estimators); local outlier factor [64] ( $k = 20$ ); PCA reconstruction error  $s_{\text{PCA}} = \min_c \|\mathbf{e} - \mathbf{P}_c \mathbf{P}_c^\top \mathbf{e}\|_2$  with  $\mathbf{P}_c$  the orthonormal projection onto the class- $c$  PCA subspace.

*d. Hybrid family (2 scores).* Hierarchical Entropy Combination:  $s_{\text{HEC}} = aH_f + bH_c + gh_i$  with  $(a, b, g) = (1.0, 0.5, 1.0)$ ,  $H_f$  and  $H_c$  the fine/coarse softmax entropies, and  $h_i = 1 - p_c[\pi(\hat{y}_f)]$  the parent-child inconsistency. Manifold Residual Score:  $s_{\text{MRS}} = \min_c \|\mathbf{e} - \text{recon}_c(\mathbf{e})\|_2$  using per-class PCA with  $k = 12$  components.

*e. Score normalisation and LightGBM hyperparameters.* Each score is rank-normalised on the validation set to a percentile in  $[0, 1]$ . The LightGBM combiner uses 300 estimators,  $\eta = 0.05$ ,  $\text{max\_depth} = -1$ ,  $\text{num\_leaves} = 31$ , class-balanced weighting; hyperparameters were chosen by 5-fold CV on the validation set. The final feature importances rank `cosine`, `energy`, `mahal_global`, `mahal_within`, `mahal_class`, and `gmm` at the top, with `pca_recon` and `mrs` lowest.

The Spearman rank-correlation matrix between the 16 scores shows three tight high-correlation blocks – the four uncertainty scores ( $\rho > 0.96$  within), the Mahalanobis variants ( $\rho > 0.91$ ), and the density/reconstruction methods ( $\rho > 0.94$ ). This within-family redundancy is why a naive average over all 16 scores underperforms and why the decorrelated logistic-regression baseline on the three least-correlated methods  $\{\text{mahal\_global}, \text{lof}, \text{msp}\}$  already reaches AUROC 0.9394, better than any

single score; the cross-family complementarity that the gradient-boosted combiner exploits is established directly by the family ablation of Sec. V C.

*f. Full per-score benchmark.* Table XIII reports AUROC and AUPRC for the 16 individual OOD scores and the four ensemble strategies on the rare-anomaly evaluation set ( $N = 289$  vs. in-distribution validation pool of 3,339), with 95% bootstrap confidence intervals over 2000 resamples.

#### Appendix D: Dataset construction details

The full classification taxonomy of the dataset (training classes plus the out-of-distribution evaluation set) appears in Table XIV. The fine-classification head sees  $K_f = 7$  merged head classes; the coarse head groups these into  $K_c = 3$  superclasses (SN-Thermonuclear, SN-CC, Non-SN). The merging rationale — hydrogen-rich CC subtypes (II/IIn/I Ib) merged because IIb has a small training sample and the H-rich CC continuum is well-known; Ibn merged into Ibc because its narrow-He signature is not always recoverable in noisy SEDM spectra — is reflected in the “Included Subtypes” column of the table.

The raw subtype distribution of the dataset (per-object and per-spectrum, before merging) appears in Table XV. After object-level filtering ( $p_{\text{TNS}} \geq 0.5$ , no numerically duplicate spectra) and subtype merging into the  $K_f = 7$  head classes, the per-class training counts used by the fine classifier are those listed in Table XIV.

*a. Preprocessing in detail.* Each spectrum is restricted to the *observer-frame* interval  $[3850, 9000] \text{ \AA}$ , with detector edges and sky-subtraction artifacts outside this window discarded and remaining missing fluxes zero-filled with a binary validity mask. All spectra are linearly interpolated onto a uniform grid of  $L = 4096$ . The interpolated flux is then rescaled to approximately  $[0, 1]$  via the robust percentile transform  $f_{\text{norm}} = (f - p_5)/(p_{95} - p_5)$ , which preserves the relative amplitude of spectral features and the continuum shape while suppressing the influence of extreme outliers; we tested per-spectrum  $z$ -score and min-max alternatives and adopted the percentile transform for its robustness to localised high-amplitude artifacts. We also evaluated rolling-median continuum removal prior to scaling and found that retaining the continuum shape improved classification of continuum-dominated classes (AGN, TDE, SLSN) without degrading line-dominated classes; no continuum removal is therefore applied in the production pipeline. Identical preprocessing is applied across all instruments (SEDM, Keck, Gemini, DESI, SDSS, NGPS).

#### Appendix E: Classification comparison with prior work

A direct comparison against published spectral classifiers on a common test set requires retraining each classifier from scratch on the same dataset, beyond the scope of this work. We provide a partial comparison by re-evaluating ASTRANet on the 6-class taxonomy used by Xu *et al.* [16], which reported a macro F1 of 72.1% outperforming ABC-SN (macro F1 56.5%) and DASH (26, macro F1 48.1%). ASTRANet on the same 6-class taxonomy achieves 88.4% accuracy and 79.4% macro F1, improvements of +4.3 pp accuracy and +7.3 pp macro F1 over the strongest prior baseline. The largest gains are on the non-SN classes.

#### Appendix F: Ablation study

*The ablation isolates architectural components under a fixed reference data configuration; the relative comparisons between variants are the quantity of interest, and absolute values are therefore not directly comparable to Sec. V A.*

To validate that each architectural and training-time component contributes, we perform leave-one-out ablations (Table XVII). Each row retrains the full model with a single component removed or replaced, keeping all other settings identical (seed = 42). All entries report best single-checkpoint performance.

Three components—hierarchical heads, multi-scale stem, and attention pooling—show marginal macro-recall improvements when removed individually. To test whether these gains are additive, we train pairwise and triple combinations of their removal (Table XVIII).

While removing individual components can boost macro recall by up to +1.3 pp, the improvements do not stack: the triple removal drops macro recall below the baseline (79.9% vs. 80.3%). Crucially, the per-class breakdown reveals that apparent gains are driven by large improvements on a single class (e.g. SLSN reaches 96.0% recall in the Hierarchy + Multi-scale ablation), while rare classes such as TDE (78.7  $\rightarrow$  72.3%), AGN (77.8  $\rightarrow$  73.3%), and CV (86.1  $\rightarrow$  84.4%) consistently degrade. Since our science goal requires reliable identification of *all* transient classes—particularly rare events like TDE—we retain the full architecture, which achieves the most balanced per-class performance.

#### Appendix G: Ensemble Strategy Comparison for Classification

*The comparison uses a fixed reference data configuration to isolate the effect of the ensembling strategy; within-seed averaging is the deployed choice, with deployment numbers in Sec. V A.*

TABLE XIII. OOD detection performance on the rare-anomaly evaluation set ( $N = 289$  rare/peculiar/out-of-taxonomy transients vs. a held-out validation pool of 3,339 in-distribution samples). AUROC and AUPRC for the 16 individual scores and the four ensemble strategies, with 95% bootstrap confidence intervals over 2000 resamples. The best individual method (typicality) and the best ensemble are highlighted; within-class Mahalanobis delivers the highest AUPRC.

Method	AUROC (95% CI)	AUPRC
<i>Uncertainty-based</i>		
MSP	0.7225 [0.6889, 0.7546]	0.204
Entropy	0.7220 [0.6874, 0.7550]	0.216
ODIN	0.7201 [0.6848, 0.7536]	0.212
Energy	0.6780 [0.6389, 0.7144]	0.191
<i>Distance-based</i>		
Mahalanobis (global)	0.8737 [0.8571, 0.8905]	0.404
Mahalanobis (class)	0.8514 [0.8281, 0.8731]	0.432
Mahalanobis (within)	0.8800 [0.8568, 0.9012]	<b>0.600</b>
$k$ -NN	0.8427 [0.8196, 0.8656]	0.465
Cosine	0.8449 [0.8180, 0.8693]	0.379
<b>Typicality</b>	<b>0.8822 [0.8587, 0.9022]</b>	0.533
<i>Density-based</i>		
GMM	0.8632 [0.8408, 0.8851]	0.464
Isolation Forest	0.8749 [0.8563, 0.8910]	0.412
LOF	0.7534 [0.7222, 0.7825]	0.276
PCA reconstruction	0.8578 [0.8379, 0.8767]	0.398
<i>Hybrid</i>		
HEC	0.7372 [0.7027, 0.7693]	0.195
MRS	0.8233 [0.7977, 0.8485]	0.388
<i>Ensembles</i>		
AUROC-weighted Rank (16 methods)	0.8532	—
Decorrelated LR ({mahal_global, lof, msp})	0.8845 (CV 0.8841 $\pm$ 0.0150)	—
Logistic Regression (all 16)	0.9382 (CV 0.9358 $\pm$ 0.0141)	—
<b>LightGBM</b>	<b>0.9851 [0.9813, 0.9884]</b> (CV 0.9460 $\pm$ 0.0149)	—

The training procedure yields two checkpoints per seed (best-validation and SWA [82]); across three seeds {42, 123, 7} this gives 6 checkpoints. We compare eight strategies for combining them: three uniform-averaging baselines (cross-seed, within-seed, and a flat super-ensemble) and five strategies tuned on the validation set (cost-sensitive per-class calibration, learned per-class weights, logistic-regression stacking, selective per-class inclusion, and per-model temperature scaling). Full per-class results are in Table XIX.

*a. Baseline strategies (uniform averaging).*

- *Cross-seed ensemble:* for each seed, take the checkpoint with the highest validation macro recall and uniformly average their softmax outputs ( $M = 3$ ).
- *Within-seed ensemble:* for each seed, first uniformly average the softmax outputs of both checkpoints *within* the seed, then uniformly average the per-seed results across seeds ( $M = 6$  in total, hierarchically averaged).
- *Super-ensemble:* uniformly average the softmax outputs of all 6 checkpoints in a single step, ignoring seed structure.

*b. Advanced strategies (tuned on validation).* The following four strategies fit hyperparameters on the validation set and are applied to the test set; the within-seed

ensemble is the unsupervised baseline against which they are compared.

- *Cost-sensitive calibration:* per-class probability scaling factors  $\mathbf{s} = (s_1, \dots, s_{K_f})$  are tuned by coordinate descent on the validation set to maximise macro recall. At inference, the prediction is  $\hat{y} = \arg \max_k s_k p_k$ .
- *Strategy 1 – Learned per-class weights:* a separate weight vector  $\mathbf{w}^{(c)} \in \Delta^{M-1}$  is learned per class, parameterised as a softmax of free logits and optimised by Nelder–Mead to maximise validation macro recall. The fine prediction is then  $\hat{y} = \arg \max_c \sum_{m=1}^M w_m^{(c)} p_c^{(m)}$ . Generalises uniform averaging by allowing different models to dominate for different classes.
- *Strategy 2 – Stacking (LogReg):* a logistic regression meta-learner is trained on the validation set with concatenated per-model softmax vectors as features ( $\mathbb{R}^{MK_f}$  feature dim.), class-balanced sample weights, and  $\ell_2$  regularisation. The regularisation strength is selected by 5-fold CV macro recall over  $C \in \{0.01, 0.1, 0.5, 1, 5, 10, 50\}$ . The meta-learner can capture non-trivial cross-model and cross-class interactions.
- *Strategy 3 – Selective per-class ensemble:* for each

TABLE XIV. Classification taxonomy and dataset composition. “Head class” is the merged label seen by the fine classification head ( $K_f = 7$ ); “Category” is the physical grouping used by the coarse head ( $K_c = 3$ ).  $N$  is the number of spectra. The OOD set is used to evaluate the framework’s ability to recognise unfamiliar transients; raw-subtype counts and additional merging detail appear in Table XV below.

Class	Head class	Category	$N$	Included Subtypes	Notes
<i>Training Classes</i>					
SN Ia	SN Ia	SN Thermo	12,973	Ia, Ia-norm, Ia-91T, Ia-91bg, Ia-02ex, Ia-03fg, Ia-pec, Ia-99aa	Ia-CSM excluded
SN II	SN II	SN CC (H)	5,166	Type II, II-norm, IIP, IIL, II-pec	—
SN IIn	SN II	SN CC (H)	1,191	IIn, Ia-CSM	Ia-CSM: H $\alpha$ emission
SN IIb	SN II	SN CC (H)	791	IIb	—
SN Ibc	SN Ibc	SN CC (SE)	2,972	Ib, Ic, Ib/c, Ic-BL, Ib-pec, Icn, Ien	Without SLSN or Ibn
SN Ibn	SN Ibc	SN CC (SE)	243	Ibn	Narrow He, spectrally unique
SLSN	SLSN	SN Lumin	835	Ic-SLSN, II-SLSN, SLSN I, Ic.5-SLSN	10–100 $\times$ luminous
AGN	AGN	Non-SN	494	AGN, Seyfert, Gal. Nuclei	Seyfert-type only
TDE	TDE	Non-SN	848	Tidal Disruption Event	—
CV	CV	Non-SN	765	Cataclysmic, U Gem, AM CVn, Nova-like	Accretion-powered
<i>Out-of-Distribution Evaluation</i>					
QSO	—	Non-SN	28	AGN Outlier	Subcategory of AGN
Blazar	—	Non-SN	11	AGN Outlier	Subcategory of AGN
BL Lac	—	Non-SN	1	AGN Outlier	Subcategory of AGN
Novae	—	Non-SN	67	CV-related	Thermonuclear runaway on WD
Classical Nova	—	Non-SN	8	CV-related	Thermonuclear runaway on WD
Afterglow	—	Non-SN	17	GRB-related	Post-GRB emission
long GRB	—	Non-SN	1	GRB-related	Stellar collapse / engine
ILRT	—	Uncertain	33	Gap transient	EC-SN or non-terminal eruption
FBOT	—	Uncertain	98	Gap transient	Engine-driven or TDE from IMBH
Ca-rich	—	SN CC (SE)	10	Peculiar SN	He-shell detonation on WD?
LRN	—	Non-SN	15	Stellar merger	Common envelope ejection
<i>Total OOD spectra (rare set):</i>					<b>289</b>

TABLE XV. Raw distribution of transient types in the dataset (Sec. III), per unique object identifier and aggregated over spectroscopic epochs. The ratio of spectra to objects reveals the typical observational cadence per class.

Type	Objects	Spectra	Type	Objects	Spectra
SN Ia	7328	12120	SN Ia-CSM	14	67
SN II	1559	4375	AM CVn	14	35
CV	392	565	FBOT	12	100
AGN	343	478	U Gem	11	15
SN II <sub>n</sub>	321	1057	Nova-like	10	91
SN Ic	282	1183	SN Ia-03fg	10	57
SN Ib	252	955	afterglow	9	19
SN II <sub>b</sub>	194	740	ILRT	8	34
SN IIP	150	307	Blazar	6	11
TDE	136	752	SLSN I	6	19
SN Ic-SLSN	97	581	Classical Nova	6	9
SN Ia-91T	86	145	Ca-rich	5	10
SN Ic-BL	83	463	SN Ib-pec	4	15
SN Ia-norm	81	133	Galactic Nuclei	3	3
SN II-SLSN	52	199	SN IIL	3	3
Novae	43	71	SN Icn	3	73
SN Ia-91bg	41	78	SN Ic.5-SLSN	2	5
SN Ibn	39	235	Luminous Red Nova	2	15
SN Ib/c	34	92	Seyfert	1	1
SN Ia-pec	26	113	SN Ien	1	19
SN II-norm	23	70	long GRB	1	1
QSO	18	29	SN II-pec	1	24
SN Ia-02cx	18	70	BL Lac	1	1
			SN Ia-99aa	1	1

TABLE XVI. Per-class recall comparison (%) between **ASTRANet** and the strongest prior baseline **SpectraNet** [16] on the same 6-class ZTF-derived spectroscopic taxonomy.

Class	SpectraNet	ASTRANet	$\Delta$ (pp)
SN Ia	92	95.2	+3.2
SN Ibc	73	79.7	+6.7
SN II	79	81.9	+2.9
AGN	70	71.1	+1.1
CV	72	<b>85.2</b>	<b>+13.2</b>
TDE	67	<b>76.6</b>	<b>+9.6</b>
Macro	75.5	81.6	+6.1

class  $c$ , only checkpoints whose validation per-class recall for  $c$  exceeds a threshold  $\tau_c$  are included in the average for that class. The threshold is a single global scalar swept over  $\tau \in [0, 0.85]$ , with the value maximising validation macro recall retained.

- *Strategy 4 – Temperature scaling:* a per-model temperature  $T_m$  rescales the logits before softmax,  $\mathbf{p}^{(m)} = \text{softmax}(\mathbf{z}^{(m)}/T_m)$ . Temperatures are optimised by coordinate descent on the validation set with grid  $T \in [0.3, 3.0]$ , step 0.05, for at most 5 outer iterations.

*c. Headline results.* Table XIX reports test-set accuracy, macro recall, and per-class recall for all strategies. The within-seed ensemble is the single most accurate strategy (87.5% accuracy, 82.9% macro recall, with the best recall on 4 of 7 classes: SN Ia, SN Ibc, SLSN, SN II). Stacking marginally ties the best macro recall (83.0%, +0.05 pp over within-seed) but at the cost of 2.7 pp in accuracy, driven by overfitting of the meta-learner to validation idiosyncrasies. Cost-sensitive calibration and temperature scaling boost TDE recall by +4.3 and +2.1 pp respectively but degrade SN Ibc, SN II, and overall accuracy. The remaining strategies are within  $\pm 1$  pp of the within-seed baseline across all metrics.

*d. Diagnostics: why advanced strategies do not improve over within-seed.* We attribute the marginal returns of the advanced strategies to three factors:

1. *Ensemble component correlation.* The 6 checkpoints are derived from 3 seeds of a single architecture revision and share data augmentation, loss function, and optimisation schedule. Their softmax distributions are highly correlated (mean off-diagonal Spearman  $\rho \approx 0.96$  on the test set), leaving little headroom for learned weighting schemes.
2. *Validation–test distribution shift.* Per-model recall on the rarest classes (TDE, AGN, SLSN) has small-sample variance: with  $N_{\text{val}}^{(\text{TDE})} = 42$  and  $N_{\text{val}}^{(\text{AGN})} = 43$ , a hyperparameter tuned to a 5% validation recall improvement is generically within bootstrap noise on the test set.
3. *Macro-recall plateau.* The within-seed and stacking strategies tie at macro recall  $\sim 83\%$ , while

the single-best seed-123 checkpoint already reaches macro recall 83.0% at 86.3% accuracy. The implication is that the residual classification errors are driven by intrinsic spectral overlap (Ibc/II, AGN/TDE), not by ensemble suboptimality. We confirm this in the per-class confusion structure (Fig. 2): off-diagonal mass concentrates on the physically expected confusions, and reshuffling ensemble weights only redistributes errors within those off-diagonal blocks.

*e. Choice of operating regime.* For different deployment contexts we recommend:

- *Default deployment* (highest overall accuracy, balanced per-class performance): within-seed ensemble.
- *TDE-priority follow-up* (maximise TDE recall, accept modest accuracy loss): cost-sensitive calibration (TDE = 83.0% at 85.7% accuracy) or the single-best seed 123 checkpoint (TDE = 83.0% at 86.3% accuracy).
- *Pure ranking applications* (no hard threshold required): within-seed softmax averaging directly, with no calibration.

For all results in the main text (Sec. V A, Sec. V) we use the within-seed ensemble.

## Appendix H: Embedding-space retrieval: nearest-neighbor analogs

The SupCon objective (Sec. IV A) makes the 192-dimensional embedding an explicitly metric-learned space, which supports similarity search as a by-product of the framework. Two diagnostics quantify this.

(i) *The embedding alone carries the classification.* A bare  $k$ -nearest-neighbor classifier (cosine distance,  $k = 15$ ) over the test-set embeddings reaches 86.8% five-fold accuracy – statistically indistinguishable from the full hierarchical classifier head (86.6%, Sec. V A). The class structure visible in the UMAP projection is therefore metrically faithful, not a visualization artifact.

The same retrieval operates in two complementary regimes (Fig. 6).

(ii) *In-distribution retrieval.* For a query drawn from a trained class the neighborhood is tight and class-consistent: a SLSN query (Fig. 6a) returns SLSN neighbors at cosine distances of 0.12–0.13, i.e. a working “find more like this” filter over the archive.

(iii) *Anomaly  $\rightarrow$  analogs.* For a spectrum flagged by **ASTRANet-Sentinel**, the same retrieval answers the natural follow-up question – *what does it most resemble?* – and hands the human vetter an interpretable neighborhood instead of a bare anomaly score. An FBOT from the rare evaluation set (Fig. 6b; never seen in training)

TABLE XVII. Leave-one-out ablation study. Accuracy and macro recall on the held-out test set when individual components are removed.

Configuration	Accuracy	Macro recall
Full ASTRANet	83.2%	80.3%
– FiLM conditioning	83.4%	79.3% (−1.0)
– Hierarchical heads (flat 7-class)	84.0%	81.0% (+0.7)
– Confusion penalty	86.2%	80.7% (+0.4)
– SupCon loss	83.5%	79.9% (−0.4)
– Multi-scale stem (single $k=31$ )	85.4%	81.5% (+1.2)
– Attention pool (global avg. pool)	85.2%	81.6% (+1.3)
– MixUp	84.1%	78.4% (−1.9)

TABLE XVIII. Combined ablation of the three components that individually showed improvement when removed. Per-class recall reveals that apparent macro gains come at the expense of rare-class performance.

Configuration	Acc	Macro	Ia	Ibc	SLSN	II	AGN	CV	TDE
Full ASTRANet	83.2	80.3	92.9	71.0	84.0	71.3	77.8	86.1	<b>78.7</b>
– Hierarchy	84.0	81.0	93.0	70.6	<b>92.0</b>	74.2	77.8	85.2	74.5
– Multi-scale	85.4	81.5	93.4	<b>73.1</b>	84.0	<b>77.1</b>	77.8	86.1	<b>78.7</b>
– AttnPool	85.2	81.6	<b>93.9</b>	72.2	88.0	76.2	77.8	86.9	76.6
– Hier. + Multi.	83.8	81.6	93.6	70.6	<b>96.0</b>	72.4	77.8	84.4	76.6
– Multi. + AttnPool	83.4	80.2	93.4	69.4	88.0	71.8	75.6	88.5	74.5
– Hier. + AttnPool	84.4	81.4	93.5	71.0	92.0	74.8	77.8	84.4	76.6
– All three	86.7	79.9	94.2	72.9	80.0	81.2	73.3	85.2	72.3

sits almost twice as far from its nearest known neighbors (0.21–0.24) as the in-distribution query, and those neighbors are stripped-envelope and hydrogen-rich core-collapse spectra – precisely the ambiguous-progenitor degeneracy of Regime IV (Sec. VII D), now made explicit as a ranked list of named objects. The neighbor distance itself is thus a second, geometry-based novelty signal that corroborates the Sentinel score. In survey operation this retrieval step runs on the same cached embeddings as the Sentinel at negligible cost; scaling beyond  $\sim 10^5$  archived spectra requires only a standard approximate nearest-neighbor index.

TABLE XIX. Test-set performance for all ensemble strategies. Per-class values are recall (%). Strategies below the mid-rule are tuned on the validation set. “Models” denotes the number of softmax distributions averaged; for advanced strategies tuned on validation,  $M=6$  throughout. Best value in each column is shown in **bold**.

Strategy	Models	Acc (%)	Macro (%)	Ia	Ibc	SLSN	II	AGN	CV	TDE
Single best (seed 123, standard)	1	86.3	<b>83.0</b>	94.5	74.5	92.0	78.1	77.8	81.1	<b>83.0</b>
Cross-seed ensemble	3	87.1	81.1	94.7	73.1	80.0	81.1	75.6	84.4	78.7
Within-seed ensemble	6	<b>87.5</b>	82.9	<b>95.3</b>	<b>75.2</b>	92.0	<b>80.7</b>	75.6	82.8	78.7
Super-ensemble	6	87.1	82.3	95.1	74.5	88.0	79.7	75.6	84.4	78.7
Cost-sensitive calibration	6	85.7	82.7	94.7	71.0	<b>96.0</b>	76.9	75.6	82.0	<b>83.0</b>
Per-class weights	6	87.1	82.3	95.1	74.5	88.0	79.7	75.6	84.4	78.7
Stacking (LogReg)	6	84.9	<b>83.0</b>	92.3	71.7	92.0	76.6	73.3	<b>95.9</b>	78.7
Selective per-class	6	87.0	82.0	94.9	73.6	88.0	80.4	75.6	82.8	78.7
Temperature scaling	6	86.1	81.7	94.3	73.6	84.0	77.8	75.6	86.1	80.9

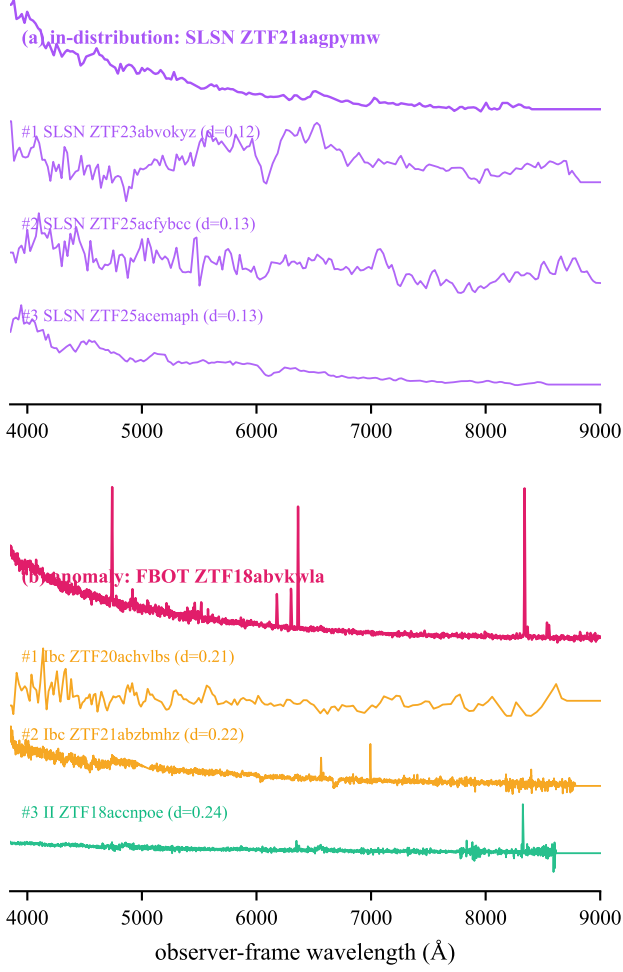


FIG. 6. Embedding-space nearest-neighbor retrieval, both regimes. In each panel the accented top spectrum is the query and the spectra below are its nearest archive neighbors by cosine distance in the **ASTRANet** embedding, coloured and labelled by their true class ( $d = \text{cosine distance}$ ). (a) *In-distribution*: a SLSN query returns SLSN neighbors at  $d \approx 0.12$  – a class-consistent “find more like this” search. (b) *Anomaly*: an FBOT flagged by **ASTRANet-Sentinel** and absent from training lies at  $d \approx 0.22$  from stripped-envelope / H-rich core-collapse neighbors, making the Regime-IV progenitor ambiguity explicit; the larger neighbor distance is itself a novelty signal. Fluxes are min-max scaled and vertically offset for display.

- [1] E. C. Bellm, S. R. Kulkarni, M. J. Graham, R. Dekany, R. M. Smith, R. Riddle, F. J. Masci, G. Helou, T. A. Prince, S. M. Adams, C. Barbarino, T. Barlow, J. Bauer, R. Beck, J. Belicki, R. Biswas, N. Blagorodnova, D. Bodewits, B. Bolin, V. Brinnel, T. Brooke, B. Bue, M. Bulla, R. Burruss, S. B. Cenko, C.-K. Chang, A. Connolly, M. Coughlin, J. Cromer, V. Cunningham, K. De, A. Delacroix, V. Desai, D. A. Duev, G. Eadie, T. L. Farnham, M. Feeney, U. Feindt, D. Flynn, A. Franckowiak, S. Frederick, C. Fremling, A. Gal-Yam, S. Gezari, M. Giomi, D. A. Goldstein, V. Z. Golkhou, A. Goobar, S. Groom, E. Hacquard, D. Hale, J. Henning, A. Y. Q. Ho, D. Hover, J. Howell, T. Hung, D. Huppenkothen, D. Imel, W.-H. Ip, Ž. Ivezić, E. Jackson, L. Jones, M. Juric, M. M. Kasliwal, S. Kaspi, S. Kaye, M. S. P. Kelley, M. Kowalski, E. Kramer, T. Kupfer, W. Landry, R. R. Laher, C.-D. Lee, H. W. Lin, Z.-Y. Lin, R. Lunnan, M. Giomi, A. Mahabal, P. Mao, A. A. Miller, S. Monkewitz, P. Murphy, C.-C. Ngeow, J. Nordin, P. Nugent, E. Ofek, M. T. Patterson, B. Penprase, M. Porter, L. Rauch, U. Rebbapragada, D. Reiley, M. Rigault, H. Rodriguez, J. van Roestel, B. Rusholme, J. van Santen, S. Schulze, D. L. Shupe, L. P. Singer, M. T. Soumagnac, R. Stein, J. Surace, J. Sollerman, P. Szkody, F. Taddia, S. Terek, A. Van Sistine, S. van Velzen, W. T. Vestrand, R. Walters, C. Ward, Q.-Z. Ye, P.-C. Yu, L. Yan, and J. Zolkower, *PASP* **131**, 018002 (2019), arXiv:1902.01932 [astro-ph.IM].
- [2] F. J. Masci, R. R. Laher, B. Rusholme, D. L. Shupe, S. Groom, J. Surace, E. Jackson, S. Monkewitz, R. Beck, D. Flynn, S. Terek, W. Landry, E. Hacquard, V. Desai, J. Howell, T. Brooke, D. Imel, S. Wachter, Q.-Z. Ye, H.-W. Lin, S. B. Cenko, V. Cunningham, U. Rebbapragada, B. Bue, A. A. Miller, A. Mahabal, E. C. Bellm, M. T. Patterson, M. Jurić, V. Z. Golkhou, E. O. Ofek, R. Walters, M. Graham, M. M. Kasliwal, R. G. Dekany, T. Kupfer, K. Burdge, C. B. Cannella, T. Barlow, A. Van Sistine, M. Giomi, C. Fremling, N. Blagorodnova, D. Levitan, R. Riddle, R. M. Smith, G. Helou, T. A. Prince, and S. R. Kulkarni, *PASP* **131**, 018003 (2019), arXiv:1902.01872 [astro-ph.IM].
- [3] M. J. Graham, S. R. Kulkarni, E. C. Bellm, S. M. Adams, C. Barbarino, N. Blagorodnova, D. Bodewits, B. Bolin, P. R. Brady, S. B. Cenko, C.-K. Chang, M. W. Coughlin, K. De, G. Eadie, T. L. Farnham, U. Feindt, A. Franckowiak, C. Fremling, S. Gezari, S. Ghosh, D. A. Goldstein, V. Z. Golkhou, A. Goobar, A. Y. Q. Ho, D. Huppenkothen, Ž. Ivezić, R. L. Jones, M. Juric, D. L. Kaplan, M. M. Kasliwal, M. S. P. Kelley, T. Kupfer, C.-D. Lee, H. W. Lin, R. Lunnan, A. A. Mahabal, A. A. Miller, C.-C. Ngeow, P. Nugent, E. O. Ofek, T. A. Prince, L. Rauch, J. van Roestel, S. Schulze, L. P. Singer, J. Sollerman, F. Taddia, L. Yan, Q.-Z. Ye, P.-C. Yu, T. Barlow, J. Bauer, R. Beck, J. Belicki, R. Biswas, V. Brinnel, T. Brooke, B. Bue, M. Bulla, R. Burruss, A. Connolly, J. Cromer, V. Cunningham, R. Dekany, A. Delacroix, V. Desai, D. A. Duev, M. Feeney, D. Flynn, S. Frederick, A. Gal-Yam, M. Giomi, S. Groom, E. Hacquard, D. Hale, G. Helou, J. Henning, D. Hover, L. A. Hillenbrand, J. Howell, T. Hung, D. Imel, W.-H. Ip, E. Jackson, S. Kaspi, S. Kaye, M. Kowalski, E. Kramer, M. Kuhn, W. Landry, R. R. Laher, P. Mao, F. J. Masci, S. Monkewitz, P. Murphy, J. Nordin, M. T. Patterson, B. Penprase, M. Porter, U. Rebbapragada, D. Reiley, R. Riddle, M. Rigault, H. Rodriguez, B. Rusholme, J. van Santen, D. L. Shupe, R. M. Smith, M. T. Soumagnac, R. Stein, J. Surace, P. Szkody, S. Terek, A. Van Sistine, S. van Velzen, W. T. Vestrand, R. Walters, C. Ward, C. Zhang, and J. Zolkower, *PASP* **131**, 078001 (2019), arXiv:1902.01945 [astro-ph.IM].
- [4] M. T. Patterson *et al.*, *PASP* **131**, 018001 (2019).
- [5] R. Dekany, R. M. Smith, R. Riddle, M. Feeney, M. Porter, D. Hale, J. Zolkower, J. Belicki, S. Kaye, J. Henning, R. Walters, J. Cromer, A. Delacroix, H. Rodriguez, D. J. Reiley, P. Mao, D. Hover, P. Murphy, R. Burruss, J. Baker, M. Kowalski, K. Reif, P. Mueller, E. Bellm, M. Graham, and S. R. Kulkarni, *PASP* **132**, 038001 (2020), arXiv:2008.04923 [astro-ph.IM].
- [6] Ž. Ivezić, S. M. Kahn, *et al.*, *The Astrophysical Journal* **873**, 111 (2019), arXiv:0805.2366.
- [7] N. Blagorodnova, J. D. Neill, R. Walters, S. R. Kulkarni, C. Fremling, S. Ben-Ami, R. G. Dekany, J. R. Fucik, N. Konidaris, R. Nash, C.-C. Ngeow, E. O. Ofek, D. O. Sullivan, R. Quimby, A. Ritter, and K. E. Vyhmeister, *PASP* **130**, 035003 (2018).
- [8] M. Rigault, J. D. Neill, N. Blagorodnova, A. Dugas, M. Feeney, R. Walters, V. Brinnel, Y. Copin, C. Fremling, J. Nordin, and J. Sollerman, *A&A* **627**, A115 (2019), arXiv:1902.08526 [astro-ph.IM].
- [9] R. J. Foley, P. J. Challis, R. Chornock, *et al.*, *The Astrophysical Journal* **767**, 57 (2013), arXiv:1212.2209.
- [10] H. B. Perets, A. Gal-Yam, P. A. Mazzali, D. Arnett, D. Kagan, A. V. Filippenko, W. Li, I. Arcavi, S. B. Cenko, D. B. Fox, *et al.*, *Nature* **465**, 322 (2010), arXiv:0906.2003 [astro-ph.HE].
- [11] M. R. Drout, R. Chornock, A. M. Soderberg, N. E. Sanders, R. McKinnon, A. Rest, R. J. Foley, D. Milisavljevic, R. Margutti, E. Berger, *et al.*, *The Astrophysical Journal* **794**, 23 (2014), arXiv:1405.3668 [astro-ph.HE].
- [12] A. Y. Q. Ho, D. A. Perley, A. Gal-Yam, R. Lunnan, J. Sollerman, S. Schulze, K. K. Das, D. Dobie, Y. Yao, C. Fremling, S. Adams, S. Anand, I. Andreoni, E. C. Bellm, R. J. Bruch, K. B. Burdge, A. J. Castro-Tirado, A. Dahiwal, K. De, R. Dekany, A. J. Drake, D. A. Duev, M. J. Graham, G. Helou, D. L. Kaplan, V. Karambelkar, M. M. Kasliwal, E. C. Kool, S. R. Kulkarni, A. A. Mahabal, M. S. Medford, A. A. Miller, J. Nordin, E. Ofek, G. Petitpas, R. Riddle, Y. Sharma, R. Smith, A. J. Stewart, K. Taggart, L. Tartaglia, A. Tzanidakis, and J. M. Winters, *The Astrophysical Journal* **949**, 120 (2023).
- [13] T. A. Thompson, J. L. Prieto, K. Z. Stanek, M. D. Kistler, J. F. Beacom, and C. S. Kochanek, *The Astrophysical Journal* **705**, 1364 (2009), arXiv:0809.0510 [astro-ph].
- [14] C. Fremling, X. J. Hall, M. W. Coughlin, A. S. Dahiwal, D. A. Duev, M. J. Graham, M. M. Kasliwal, E. C. Kool, A. A. Mahabal, A. A. Miller, J. D. Neill, D. A. Perley, M. Rigault, P. Rosnet, B. Rusholme, Y. Sharma, K. M. Shin, D. L. Shupe, J. Sollerman, and R. S. Walters, *ApJL* **917**, L2 (2021), arXiv:2104.12980 [astro-ph.IM].
- [15] Y. Sharma, A. A. Mahabal, J. Sollerman, C. Fremling, S. R. Kulkarni, N. Rehemtulla, A. A. Miller, M. Aubert,

- T. X. Chen, M. W. Coughlin, M. J. Graham, D. Hale, M. M. Kasliwal, Y.-L. Kim, J. D. Neill, J. N. Purdum, B. Rusholme, A. Singh, and N. Sravan, *PASP* **137**, 034507 (2025).
- [16] M. Xu, A. Sasli, A. Junell, F. F. Nunes, Y.-J. Qin, C. Fremling, S. Rose, T. J. D. Laz, B. Border, A. L. Calloch, S. S. Chaudhary, H. Markoff, A. Raghuvanshi, N. Rehemtulla, J. Sollerman, Y. Sharma, N. Sravan, J. Adler, T. X. Chen, R. Dekany, R. Riddle, M. M. Kasliwal, M. J. Graham, and M. W. Coughlin, *Applecider ii: Spectranet – a deep learning network for spectroscopic data* (2025), arXiv:2510.07215 [astro-ph.IM].
- [17] W. F. Fortino, F. B. Bianco, P. Protopapas, D. Muthukrishna, and A. Brockmeier, *Abc-sn: Attention based classifier for supernova spectra* (2025), arXiv:2507.22106 [astro-ph.IM].
- [18] D. Hendrycks and K. Gimpel, *ICLR* (2017).
- [19] C. Guo, G. Pleiss, Y. Sun, and K. Q. Weinberger, in *Proceedings of the 34th International Conference on Machine Learning (ICML)*, Proceedings of Machine Learning Research, Vol. 70 (PMLR, 2017) pp. 1321–1330, arXiv:1706.04599 [cs.LG].
- [20] M. Hein, M. Andriushchenko, and J. Bitterwolf, in *Proceedings of the IEEE/CVF Conference on Computer Vision and Pattern Recognition (CVPR)* (2019) pp. 41–50, arXiv:1812.05720 [cs.LG].
- [21] V. A. Villar, M. Cranmer, E. Berger, *et al.*, *The Astrophysical Journal Supplement Series* **255**, 24 (2021), arXiv:2103.12102.
- [22] M. V. Pruzhinskaya, K. L. Malanchev, M. V. Kornilov, *et al.*, *Monthly Notices of the Royal Astronomical Society* **489**, 3591 (2019), arXiv:1905.11516.
- [23] S. Chaimi, F. B. Bianco, and A. Mahabal, *In search of the unknown unknowns: A multi-metric distance ensemble for out of distribution anomaly detection in astronomical surveys* (2025), arXiv:2510.23702 [astro-ph.IM].
- [24] R. Gupta *et al.*, arXiv e-prints (2025), *Update with actual MCIF reference.*, 2503.00000.
- [25] E. Perez, F. Strub, H. de Vries, V. Dumoulin, and A. Courville, in *Proceedings of the AAAI Conference on Artificial Intelligence*, Vol. 32 (2018) p. N/A.
- [26] D. Muthukrishna, D. Parkinson, and B. E. Tucker, *ApJ* **885**, 85 (2019).
- [27] T. J. du Laz, M. W. Coughlin, P. Bachant, J. E. Simones, T. Culino, A. L. Calloch, S. S. Chaudhary, X. J. Hall, T. Barna, D. Warshofsky, M. Graham, M. M. Kasliwal, A. Mahabal, J. S. Bloom, A. Palmese, F. J. Masci, S. L. Groom, R. Dekany, R. L. Riddle, and G. Helou, *Boom and babamul: a real-time, multi-survey, optical alert broker system operating at scale* (2025), arXiv:2511.00164 [astro-ph.IM].
- [28] A. Junell, A. Sasli, F. F. Nunes, M. Xu, B. Border, N. Rehemtulla, M. Rizhko, Y.-J. Qin, T. J. D. Laz, A. L. Calloch, S. S. Chaudhary, S. Wu, J. Sollerman, N. Sravan, S. L. Groom, D. Hale, M. M. Kasliwal, J. Purdum, A. Wold, M. J. Graham, and M. W. Coughlin, *Applying multimodal learning to classify transient detections early (applecider) i: Data set, methods, and infrastructure* (2025), arXiv:2507.16088 [astro-ph.IM].
- [29] M. Yuksekgonul, L. Zhang, J. Zou, and C. Guestrin, *Beyond confidence: Reliable models should also consider atypicality* (2023), arXiv:2305.18262 [cs.LG].
- [30] R. Margutti, B. D. Metzger, R. Chornock, I. Vurm, N. Roth, B. W. Grefenstette, V. Savchenko, R. Cartier, J. F. Steiner, G. Terreran, *et al.*, *The Astrophysical Journal* **872**, 18 (2019), arXiv:1810.10720 [astro-ph.HE].
- [31] D. A. Perley, P. A. Mazzali, L. Yan, S. B. Cenko, S. Gezari, K. Taggart, N. Blagorodnova, C. Fremling, B. Mockler, A. Singh, *et al.*, *Monthly Notices of the Royal Astronomical Society* **484**, 1031 (2019), arXiv:1808.00969 [astro-ph.HE].
- [32] C. S. Kochanek, D. M. Szczygiel, and K. Z. Stanek, *The Astrophysical Journal* **758**, 142 (2012), arXiv:1202.0281 [astro-ph.SR].
- [33] T. Barna, C. Fremling, T. Ahumada, I. Andreoni, S. Banerjee, J. S. Bloom, M. Bulla, T. X. Chen, M. W. Coughlin, T. Dietrich, X. J. Hall, A. Junell, B. Rusholme, J. Sollerman, and N. Sravan, *Publications of the Astronomical Society of the Pacific* **137**, 084105 (2025).
- [34] C. Fremling, D. Perley, A. Y. Q. Ho, and ZTF Collaboration, *GRB Coordinates Network* **31629**, 1 (2022).
- [35] S. J. van der Walt, A. Crellin-Quick, and J. S. Bloom, *Journal of Open Source Software* **4**, 1247 (2019).
- [36] M. W. Coughlin, J. S. Bloom, G. Nir, S. Antier, T. J. du Laz, S. van der Walt, A. Crellin-Quick, T. Culino, D. A. Duev, D. A. Goldstein, B. F. Healy, V. Karambelkar, J. Lilleboe, K. M. Shin, L. P. Singer, T. Ahumada, S. Anand, E. C. Bellm, R. Dekany, M. J. Graham, M. M. Kasliwal, I. Kostadinova, R. W. Kiendrebeogo, S. R. Kulkarni, S. Jenkins, N. LeBaron, A. A. Mahabal, J. D. Neill, B. Parazin, J. Peloton, D. A. Perley, R. Riddle, B. Rusholme, J. van Santen, J. Sollerman, R. Stein, D. Turpin, A. Wold, C. Amat, A. Bonnefon, A. Bonnefoy, M. Flament, F. Kerkow, S. Kishore, S. Jani, S. K. Mahanty, C. Liu, L. Llinares, J. Makarison, A. Olliéric, I. Perez, L. Pont, and V. Sharma, *ApJS* **267**, 31 (2023), arXiv:2305.00108 [astro-ph.IM].
- [37] A. Sasli, *IRIS: Identification and Reduction of Interesting Spectra*, <https://github.com/applecider-ml/IRIS> (2026), spectral preprocessing pipeline for transient classification.
- [38] C. Fremling, A. A. Miller, Y. Sharma, A. Dugas, D. A. Perley, K. Taggart, J. Sollerman, A. Goobar, M. L. Graham, J. D. Neill, J. Nordin, M. Rigault, R. Walters, I. Andreoni, A. Bagdasaryan, J. Belicki, C. Cannella, E. C. Bellm, S. B. Cenko, K. De, R. Dekany, S. Frederick, V. Z. Golkhou, M. J. Graham, G. Helou, A. Y. Q. Ho, M. M. Kasliwal, T. Kupfer, R. R. Laher, A. Mahabal, F. J. Masci, R. Riddle, B. Rusholme, S. Schulze, D. L. Shupe, R. M. Smith, S. van Velzen, L. Yan, Y. Yao, Z. Zhuang, and S. R. Kulkarni, *ApJ* **895**, 32 (2020), arXiv:1910.12973 [astro-ph.HE].
- [39] D. A. Perley, C. Fremling, J. Sollerman, A. A. Miller, A. S. Dahiwal, Y. Sharma, E. C. Bellm, R. Biswas, T. G. Brink, R. J. Bruch, K. De, R. Dekany, A. J. Drake, D. A. Duev, A. V. Filippenko, A. Gal-Yam, A. Goobar, M. J. Graham, M. L. Graham, A. Y. Q. Ho, I. Irani, M. M. Kasliwal, Y.-L. Kim, S. R. Kulkarni, A. Mahabal, F. J. Masci, S. Modak, J. D. Neill, J. Nordin, R. L. Riddle, M. T. Soumagnac, N. L. Strotjohann, S. Schulze, K. Taggart, A. Tzanidakis, R. S. Walters, and L. Yan, *ApJ* **904**, 35 (2020).
- [40] N. Rehemtulla, A. A. Miller, T. Jegou Du Laz, M. W. Coughlin, C. Fremling, D. A. Perley, Y.-J. Qin, J. Sollerman, A. A. Mahabal, R. R. Laher, R. Riddle, B. Rusholme, and S. R. Kulkarni, *ApJ* **972**, 7 (2024), arXiv:2401.15167 [astro-ph.IM].
- [41] N. Blagorodnova, J. D. Neill, R. Walters, S. R. Kulka-

- rni, C. Fremling, S. Ben-Ami, R. G. Dekany, J. R. Fucik, N. Konidaris, R. Nash, C.-C. Ngeow, E. O. Ofek, D. O’ Sullivan, R. Quimby, A. Ritter, and K. E. Vyhmeister, *PASP* **130**, 035003 (2018), arXiv:1710.02917 [astro-ph.IM].
- [42] Y. L. Kim, M. Rigault, J. D. Neill, M. Briday, Y. Copin, J. Lezmy, N. Nicolas, R. Riddle, Y. Sharma, M. Smith, J. Sollerman, and R. Walters, *PASP* **134**, 024505 (2022), arXiv:2203.01346 [astro-ph.IM].
- [43] J. B. Oke, J. G. Cohen, M. Carr, J. Cromer, A. Dingizian, F. H. Harris, S. Labrecque, R. Lucinio, W. Schaal, H. Epps, and J. Miller, *Publications of the Astronomical Society of the Pacific* **107**, 375 (1995).
- [44] S. M. Faber, A. C. Phillips, R. I. Kibrick, B. Alcott, S. L. Allen, J. Burrous, T. Cantrall, D. Clarke, A. L. Coil, D. J. Cowley, M. Davis, W. T. S. Deich, K. Dietsch, D. K. Gilmore, C. A. Harper, D. F. Hilyard, J. P. Lewis, M. McVeigh, J. Newman, J. Osborne, R. Schiavon, R. J. Stover, D. Tucker, V. Wallace, M. Wei, G. Wirth, and C. A. Wright, in *Instrument Design and Performance for Optical/Infrared Ground-based Telescopes*, Society of Photo-Optical Instrumentation Engineers (SPIE) Conference Series, Vol. 4841, edited by M. Iye and A. F. M. Moorwood (2003) pp. 1657–1669.
- [45] R. L. Davies, J. R. Allington-Smith, P. Bettess, E. Chadwick, R. Content, G. N. Dodsworth, R. Haynes, D. Lee, I. J. Lewis, J. Webster, E. Atad, S. M. Beard, M. Ellis, P. R. Hastings, P. R. Williams, T. Bond, D. Crampton, T. J. Davidge, M. Fletcher, B. Leckie, C. L. Morbey, R. G. Murowinski, S. Roberts, L. K. Saddlemeyer, J. Sebesta, J. R. Stilburn, and K. Szeto, in *Optical Telescopes of Today and Tomorrow*, Society of Photo-Optical Instrumentation Engineers (SPIE) Conference Series, Vol. 2871, edited by A. L. Ardeberg (1997) pp. 1099–1106.
- [46] R. W. e. a. Pogge, in *SPIE*, Vol. 7735 (2010).
- [47] M. M. Kasliwal, C. Fremling, L. Yan, K. Das, F. Verdi, J. Zmudzin, C. Martin, E. Kirby, S. Xue, L. Ho, G. Herczeg, X. Wu, Z. Hu, H. Ji, M. Matuszewski, R. Bertz, D. Hale, H. Rodriguez, A. Boden, R. Dekany, R. Smith, D. Reiley, R. Nash, J. Milburn, D. Neill, J. Brugger, R. Zarzaca, B. Weber, and C. Shapiro, *Transient Name Server AstroNote* **340**, 1 (2024).
- [48] Abdurro’uf, K. Accetta, C. Aerts, V. Silva Aguirre, R. Ahumada, N. Ajgaonkar, N. Filiz Ak, S. Alam, C. Allende Prieto, A. Almeida, F. Anders, S. F. Anderson, B. H. Andrews, B. Anguiano, E. Aquino-Ortíz, A. Aragón-Salamanca, M. Argudo-Fernández, M. Ata, M. Aubert, V. Avila-Reese, C. Badenes, R. H. Barbá, K. Barger, J. K. Barrera-Ballesteros, R. L. Beaton, T. C. Beers, F. Belfiore, C. F. Bender, M. Bernardi, M. A. Bershad, F. Beutler, C. M. Bidin, J. C. Bird, D. Bizyaev, G. A. Blanc, M. R. Blanton, N. F. Boardman, A. S. Bolton, M. Boquien, J. Borissova, J. Bovy, W. N. Brandt, J. Brown, J. R. Brownstein, M. Brusa, J. Buchner, K. Bundy, J. N. Burchett, M. Bureau, A. Burgasser, T. K. Cabang, S. Campbell, M. Cappellari, J. K. Carlberg, F. C. Wanderley, R. Carrera, J. Cash, Y.-P. Chen, W.-H. Chen, B. Cherinka, C. Chiappini, P. D. Choi, S. D. Chojnowski, H. Chung, N. Clerc, R. E. Cohen, J. M. Comerford, J. Comparat, L. da Costa, K. Covey, J. D. Crane, I. Cruz-Gonzalez, C. Culhane, K. Cunha, Y. S. Dai, G. Damke, J. Darling, J. W. Davidson, Jr., R. Davies, K. Dawson, N. De Lee, A. M. Diamond-Stanic, M. Cano-Díaz, H. D. Sánchez, J. Donor, C. Duckworth, T. Dwelly, D. J. Eisenstein, Y. P. Elsworth, E. Emsellem, M. Eracleous, S. Escoffier, X. Fan, E. Farr, S. Feng, J. G. Fernández-Trincado, D. Feuillet, A. Filipp, S. P. Fillingham, P. M. Frinchaboy, S. Fromenteau, L. Galbany, R. A. García, D. A. García-Hernández, J. Ge, D. Geisler, J. Gelfand, T. Géron, B. J. Gibson, J. Goddy, D. Godoy-Rivera, K. Grabowski, P. J. Green, M. Greener, C. J. Grier, E. Griffith, H. Guo, J. Guy, M. Hadjara, P. Harding, S. Hasselquist, C. R. Hayes, F. Hearty, J. Hernández, L. Hill, D. W. Hogg, J. A. Holtzman, D. Horta, B.-C. Hsieh, C.-H. Hsu, Y.-H. Hsu, D. Huber, M. Huertas-Company, B. Hutchinson, H. S. Hwang, H. J. Ibarra-Medel, J. I. Chitham, G. S. Ilha, J. Imig, W. Jaekle, T. Jayasinghe, X. Ji, J. A. Johnson, A. Jones, H. Jönsson, I. Katkov, A. Khalatyan, Dr., K. Kinemuchi, S. Kisku, J. H. Knapen, J.-P. Kneib, J. A. Kollmeier, M. Kong, M. Kounkel, K. Kreckel, D. Krishnarao, I. Lacerna, R. R. Lane, R. Langgin, R. Lavender, D. R. Law, D. Lazarz, H. W. Leung, H.-H. Leung, H. M. Lewis, C. Li, R. Li, J. Lian, F.-H. Liang, L. Lin, Y.-T. Lin, S. Lin, C. Lintott, D. Long, P. Longa-Peña, C. López-Cobá, S. Lu, B. F. Lundgren, Y. Luo, J. T. Mackereth, A. de la Macorra, S. Mahadevan, S. R. Majewski, A. Manchado, T. Mandeville, C. Maraston, B. Margalef-Bentabol, T. Masseron, K. L. Masters, S. Mathur, R. M. McDermid, M. Mckay, A. Merloni, M. Merrifield, S. Meszaros, A. Miglio, F. Di Mille, D. Minniti, R. Minsley, and A. Monachesi, *ApJS* **259**, 35 (2022), arXiv:2112.02026 [astro-ph.GA].
- [49] DESI Collaboration, A. G. Adame, J. Aguilar, S. Ahlen, S. Alam, G. Aldering, D. M. Alexander, R. Alfarsy, C. Allende Prieto, M. Alvarez, O. Alves, A. Anand, F. Andrade-Oliveira, E. Armengaud, J. Asorey, S. Avila, A. Aviles, S. Bailey, A. Balaguera-Antolínez, O. Ballester, C. Baltay, A. Bault, J. Bautista, J. Behera, S. F. Beltran, S. BenZvi, L. Beraldo e Silva, J. R. Bermejo-Climent, A. Berti, R. Besuner, F. Beutler, D. Bianchi, C. Blake, R. Blum, A. S. Bolton, S. Brieden, A. Brodzeller, D. Brooks, Z. Brown, E. Buckley-Geer, E. Burtin, L. Cabayol-Garcia, Z. Cai, R. Canning, L. Cardiel-Sas, A. Carnero Rosell, F. J. Castander, J. L. Cervantes-Cota, S. Chabanier, E. Chaussidon, J. Chaves-Montero, S. Chen, X. Chen, C. Chuang, T. Claybaugh, S. Cole, A. P. Cooper, A. Cuceu, T. M. Davis, K. Dawson, R. de Belsunce, R. de la Cruz, A. de la Macorra, J. Della Costa, A. de Mattia, R. Demina, U. Demirbozan, J. DeRose, A. Dey, B. Dey, G. Dhungana, J. Ding, Z. Ding, P. Doel, R. Doshi, K. Douglass, A. Edge, S. Eftekharzadeh, D. J. Eisenstein, A. Elliott, J. Ereza, S. Escoffier, P. Fagrellius, X. Fan, K. Fanning, V. A. Fawcett, S. Ferraro, B. Flaugher, A. Font-Ribera, J. E. Forero-Romero, D. Forero-Sánchez, C. S. Frenk, B. T. Gänsicke, L. Á. García, J. García-Bellido, C. Garcia-Quintero, L. H. Garrison, H. Gil-Marín, J. Golden-Marx, S. Gontcho A Gontcho, A. X. Gonzalez-Morales, V. Gonzalez-Perez, C. Gordon, O. Graur, D. Green, D. Gruen, J. Guy, B. Hadzhiyska, C. Hahn, J. J. Han, M. M. S. Hanif, H. K. Herrera-Alcantar, K. Honscheid, J. Hou, C. Howlett, D. Huterer, V. Iršič, M. Ishak, A. Jacques, A. Jana, L. Jiang, J. Jimenez, Y. P. Jing, S. Joudaki, R. Joyce, E. Jullo, S. Juneau, N. G. Karaçaylı, T. Karim, R. Kehoe, S. Kent, A. Khederlarian, S. Kim, D. Kirkby, T. Kisner, F. Kitaura, N. Kizhuprakkat, J. Kneib,

- S. E. Koposov, A. Kovács, A. Kremin, A. Krolewski, B. L'Huillier, O. Lahav, A. Lambert, C. Lamman, T. W. Lan, M. Landriau, D. Lang, J. U. Lange, J. Lasker, A. Leauthaud, L. Le Guillou, M. E. Levi, T. S. Li, E. Linder, A. Lyons, C. Magneville, M. Manera, C. J. Manser, D. Margala, P. Martini, P. McDonald, G. E. Medina, L. Medina-Varela, A. Meisner, J. Mena-Fernández, J. Meneses-Rizo, M. Mezcuca, R. Miquel, P. Montero-Camacho, J. Moon, S. Moore, J. Moustakas, E. Mueller, J. Mundet, A. Muñoz-Gutiérrez, A. D. Myers, S. Nadathur, L. Napolitano, R. Neveux, J. A. Newman, J. Nie, R. Nikutta, G. Niz, P. Norberg, H. E. Noriega, E. Paillas, N. Palanque-Delabrouille, A. Palmese, Z. Pan, D. Parkinson, S. Penmetsa, W. J. Percival, A. Pérez-Fernández, I. Pérez-Ràfols, M. Pieri, C. Poppett, A. Porredon, and S. Pothier, *AJ* **168**, 58 (2024), arXiv:2306.06308 [astro-ph.CO].
- [50] M. M. Kasliwal, C. Cannella, A. Bagdasaryan, T. Hung, U. Feindt, L. P. Singer, M. Coughlin, C. Fremling, R. Walters, D. Duev, R. Itoh, and R. M. Quimby, *PASP* **131**, 038003 (2019).
- [51] D. A. Coulter, D. O. Jones, P. McGill, R. J. Foley, P. D. Aleo, M. J. Bustamante-Rosell, D. Chatterjee, K. W. Davis, C. Dickinson, A. Engel, A. Gagliano, W. V. Jacobson-Galán, C. D. Kilpatrick, J. Kutcka, X. K. Le Saux, K. Malanchev, Y. C. Pan, P. J. Quiñonez, C. Rojas-Bravo, M. R. Siebert, K. Taggart, S. Tinyanont, and Q. Wang, *PASP* **135**, 064501 (2023), arXiv:2303.02154 [astro-ph.IM].
- [52] S. Bai, J. Z. Kolter, and V. Koltun, arXiv preprint arXiv:1803.01271 (2018).
- [53] M. Ilse, J. M. Tomczak, and M. Welling, in *International Conference on Machine Learning (ICML)* (PMLR, 2018) pp. 2127–2136.
- [54] P. Khosla, P. Teterwak, C. Wang, A. Sarna, Y. Tian, P. Isola, A. Maschinot, C. Liu, and D. Krishnan, in *Advances in Neural Information Processing Systems (NeurIPS)*, Vol. 33 (2020) pp. 18661–18673.
- [55] T.-Y. Lin, P. Goyal, R. Girshick, K. He, and P. Dollár, in *Proceedings of the IEEE International Conference on Computer Vision (ICCV)* (2017) pp. 2980–2988.
- [56] I. Loshchilov and F. Hutter, in *International Conference on Learning Representations (ICLR)* (2019).
- [57] H. Zhang, M. Cisse, Y. N. Dauphin, and D. Lopez-Paz, in *International Conference on Learning Representations (ICLR)* (2018).
- [58] Y. Cui, M. Jia, T.-Y. Lin, Y. Song, and S. Belongie, in *Proceedings of the IEEE/CVF Conference on Computer Vision and Pattern Recognition (CVPR)* (2019) pp. 9268–9277.
- [59] B. Lakshminarayanan, A. Pritzel, and C. Blundell, in *Advances in Neural Information Processing Systems 30 (NIPS 2017)* (2017) pp. 6402–6413, arXiv:1612.01474 [stat.ML].
- [60] S. Liang, Y. Li, and R. Srikant, Enhancing the reliability of out-of-distribution image detection in neural networks (2020), arXiv:1706.02690 [cs.LG].
- [61] W. Liu, X. Wang, J. Owens, and Y. Li, *NeurIPS* (2020).
- [62] K. Lee *et al.*, *NeurIPS* (2018).
- [63] F. T. Liu, K. M. Ting, and Z.-H. Zhou, in *Proceedings of the 8th IEEE International Conference on Data Mining (ICDM)* (IEEE Computer Society, 2008) pp. 413–422.
- [64] M. M. Breunig, H.-P. Kriegel, R. T. Ng, and J. Sander, in *Proceedings of the 2000 ACM SIGMOD International Conference on Management of Data* (ACM, 2000) pp. 93–104.
- [65] G. Ke, Q. Meng, T. Finley, T. Wang, W. Chen, W. Ma, Q. Ye, and T.-Y. Liu, in *Advances in Neural Information Processing Systems 30 (NIPS 2017)* (2017) pp. 3146–3154.
- [66] D. Hendrycks, M. Mazeika, and T. Dietterich, in *International Conference on Learning Representations (ICLR)* (2019) arXiv:1812.04606.
- [67] V. Vovk, A. Gammerman, and G. Shafer, *Algorithmic Learning in a Random World* (Springer, New York, 2005).
- [68] A. N. Angelopoulos and S. Bates, *Foundations and Trends in Machine Learning* **16**, 494 (2023).
- [69] Y. Romano, M. Sesia, and E. J. Candès, in *Advances in Neural Information Processing Systems (NeurIPS)* (2020) arXiv:2006.02544.
- [70] M. L. Li, A. Y. Q. Ho, G. Ryan, D. A. Perley, G. P. Lamb, A. J. Nayana, I. Andreoni, G. C. Anupama, E. C. Bellm, E. Berger, J. S. Bloom, E. Burns, I. Caiazzo, P. Chandra, M. W. Coughlin, K. El-Badry, M. J. Graham, M. Kasliwal, G. K. Keating, S. R. Kulkarni, H. Kumar, F. J. Masci, R. A. Perley, J. Purdum, R. Rao, A. C. Rodriguez, B. Rusholme, N. Sarin, J. Sollerman, G. P. Srinivasaragavan, V. Swain, and Z. Vanderbosch, *ApJ* **985**, 124 (2025), arXiv:2411.07973 [astro-ph.HE].
- [71] S. Chaini, A. Mahabal, A. Kembhavi, and F. Bianco, *Astronomy and Computing* **48**, 100850 (2024).
- [72] E. Swann, M. Sullivan, D. Carollo, *et al.*, *The Messenger* **175**, 58 (2019), arXiv:1903.02476.
- [73] C. Frohmaier, M. Sullivan, K. Maguire, *et al.*, in *Proceedings of SPIE*, Vol. 13096 (2024) p. 130963X.
- [74] P. Schipani, S. Campana, R. Claudi, *et al.*, in *Proceedings of SPIE*, Vol. 11447 (2020) p. 1144709.
- [75] P. J. Groot, S. Scaringi, and N. Elias-Rosa, arXiv e-prints, arXiv:2512.17404 (2025), arXiv:2512.17404 [astro-ph.IM].
- [76] A. Savitzky and M. J. E. Golay, *Analytical Chemistry* **36**, 1627 (1964).
- [77] Y. Wu and K. He, in *European Conference on Computer Vision (ECCV)* (Springer, 2018) pp. 3–19.
- [78] D. Hendrycks and K. Gimpel, arXiv preprint arXiv:1606.08415 (2016).
- [79] G. Huang, Y. Sun, Z. Liu, D. Sedra, and K. Q. Weinberger, in *European Conference on Computer Vision (ECCV)* (Springer, 2016) pp. 646–661.
- [80] I. Loshchilov and F. Hutter, in *International Conference on Learning Representations (ICLR)* (2017).
- [81] B. T. Polyak and A. B. Juditsky, *SIAM Journal on Control and Optimization* **30**, 838 (1992).
- [82] P. Izmailov, D. Podoprikin, T. Garipov, D. Vetrov, and A. G. Wilson, in *Proceedings of the Thirty-Fourth Conference on Uncertainty in Artificial Intelligence (UAI)* (2018) pp. 876–885, arXiv:1803.05407 [cs.LG].